CANCER

Tumor-associated fibrosis impairs immune surveillance and response to immune checkpoint blockade in non–small cell lung cancer

Brett H. Herzog[1,2], John M. Baer[1], Nicholas Borcherding[3], Natalie L. Kingston[1], Jad I. Belle[1], Brett L. Knolhoff[1], Graham D. Hogg[1], Faiz Ahmad[1], Liang-I Kang[3], Jessica Petrone[3], Chieh-Yu Lin[3], Ramaswamy Govindan[1,2], David G. DeNardo[2,3,4]*

Non–small cell lung cancer (NSCLC) is a leading cause of cancer-related deaths. Immune checkpoint blockade has improved survival for many patients with NSCLC, but most fail to obtain long-term benefit. Understanding the factors leading to reduced immune surveillance in NSCLC is critical in improving patient outcomes. Here, we show that human NSCLC harbors large amounts of fibrosis that correlates with reduced T cell infiltration. In murine NSCLC models, the induction of fibrosis led to increased lung cancer progression, impaired T cell immune surveillance, and failure of immune checkpoint blockade efficacy. Associated with these changes, we observed that fibrosis leads to numerically and functionally impaired dendritic cells and altered macrophage phenotypes that likely contribute to immunosuppression. Within cancer-associated fibroblasts, distinct changes within the *Col13a1*-expressing population suggest that these cells produce chemokines to recruit macrophages and regulatory T cells while limiting recruitment of dendritic cells and T cells. Targeting fibrosis through transforming growth factor–β receptor signaling overcame the effects of fibrosis to enhance T cell responses and improved the efficacy of immune checkpoint blockade but only in the context of chemotherapy. Together, these data suggest that fibrosis in NSCLC leads to reduced immune surveillance and poor responsiveness to checkpoint blockade and highlight antifibrotic therapies as a candidate strategy to overcome immunotherapeutic resistance.

INTRODUCTION

Lung cancer is the leading cause of cancer-related mortality (*1*, *2*). Non–small cell lung cancer (NSCLC) is the most encountered type of lung cancer. Current NSCLC treatments focus on tumor cell intrinsic susceptibilities, such as *EGFR* mutations, or tumor-expressed immune checkpoints, such as programmed death-ligand 1 (PD-L1) and its receptor, programmed cell death-1 (PD-1). Immune checkpoint blockade either alone or combined with traditional chemotherapy has markedly improved the survival for patients with NSCLC (*3*–*5*). However, despite the observed benefit in NSCLC, not all patients respond to these agents, and most of those who do respond eventually progress, demonstrating a need for improving treatment strategies.

Understanding why some patients have durable responses to immune checkpoint blockade and still others do not is of considerable clinical interest. Attempts at predicting benefit from immune checkpoint blockade based on tumor mutational burden alone have not borne out (*6*, *7*). However, evidence suggests that patients whose cancer cells harbor certain mutations, such as *STK11/LKB1* and *KRAS*, are less likely to obtain clinical benefit from PD-1–PD-L1 immune checkpoint blockade compared with those who harbor *KRAS* mutations alone (*8*). This suggests that certain tumor-intrinsic properties do affect response to immune checkpoint blockade for some patients. However, in addition to these tumor-intrinsic features, the tumor microenvironment (TME) is garnering increased attention as a critical determinant of response to both cancer cell–intrinsic and immune-based therapies (*9*, *10*). The TME is composed of numerous cell types, including various immune cells, endothelial cells, and fibroblasts. Many groups have attempted to identify a critical marker of response to immune checkpoint blockade within the TME. Much of the work thus far has focused on whether a tumor is "T cell inflamed," having both infiltrating T cells and a type I interferon signature or not (*11*–*14*). Several studies have demonstrated the importance of a properly activated innate sensing mechanism whereby antigen-presenting cells, such as dendritic cells, are recruited to the TME. Specifically, $CD103^+$ dendritic cells are critical to an adequate antitumor immune response because they traffic to the tumor-draining lymph node to present tumor-specific and tumor-associated antigens to T cells and produce a type I interferon response (*15*–*18*). The effector T cells must then be recruited back to the TME through the vasculature; two chemokines have been identified as critical to this process, CXCL9 and CXCL10, which are ligands for CXCR3 expressed on T cells (*19*, *20*). Together, these data suggest that one way that tumors avoid antitumor responses is through dysfunctional dendritic cells and limited T cell infiltration. Even in patients with high numbers of infiltrating T cells, dysfunction and suppression of these cells have been suggested as an additional mechanism of resistance to PD-1–PD-L1 checkpoint blockade. In addition to the PD-1–PD-L1 checkpoint, which is the most targeted checkpoint in human cancers, other coinhibitory checkpoints can be expressed by cells within the TME to limit the function of T cells (*21*, *22*). Cells such as regulatory T cells (T_{regs})

[1]Department of Medicine, Washington University School of Medicine, St. Louis, MO 63110, USA. [2]Siteman Cancer Center, Washington University School of Medicine, St. Louis, MO 63110, USA. [3]Department of Pathology and Immunology, Washington University School of Medicine, St. Louis, MO 63110, USA. [4]Department of Surgery, Washington University School of Medicine, St. Louis, MO 63110, USA.
*Corresponding author: Email: ddenardo@wustl.edu

and macrophages can also suppress the function of T cells within the TME. T_{regs} are abundant in the lung cancer TME and have been shown to limit T cell function through various mechanisms (*23*, *24*). The role of macrophages within the TME has also been explored, and, although much remains to be determined about the best way to target tumor-supporting macrophages, it is clear that a subset of macrophages play a critical role in suppressing the immune system's response to cancer development and in promoting tumor progression (*25*–*27*).

Despite our advances in understanding the role that the vasculature and immune components play in generating and delivering an effective antitumor immune response, our understanding of the impact of fibrosis remains more limited. Fibrosis includes diverse fibroblast populations and extracellular matrix (ECM) deposition, which has been shown to affect tumor immunity in some cancers (*28*–*30*). For example, fibrosis in pancreatic cancer may limit dendritic cell trafficking and function within the TME (*28*, *29*, *31*, *32*). Further, depletion of certain subsets of cancer-associated fibroblasts (CAFs) leads to acceleration of tumor progression (*33*), whereas other CAF subsets appear to restrain tumor growth in this same cancer (*31*). Tumor-associated fibrosis is associated with advanced disease and with poor prognosis in several cancer types, including NSCLC (*28*, *34*–*38*). Smoking cigarettes is a well-established risk factor for developing NSCLC and is associated with a fibrotic remodeling of the lung (*39*). In addition, idiopathic pulmonary fibrosis increases the risk of developing lung cancer (*40*). Recent studies in human NSCLC have identified different fibroblast subsets and their impact on response to therapies targeting driver mutations (*9*, *41*, *42*). Collagen, a component of fibrosis, has recently been shown to induce $CD8^+$ T cell exhaustion in models of lung cancer (*43*). However, the impact of fibrosis on immune surveillance and response to immune-based therapies in NSCLC remains largely unknown.

Here, we observed that, in human NSCLC, the degree of stromal fibrosis negatively correlates with T cell responses. In models of experimental lung fibrosis, we observed accelerated lung adenocarcinoma progression, impaired immune surveillance, and loss of responsiveness to immune checkpoint blockade. NSCLC fibrosis was associated with immunosuppressive changes in the TME that are at least in part related to transforming growth factor–β (TGFβ) signaling. Targeting fibrosis restored T cell infiltration into the NSCLC TME and improves response to immune checkpoint blockade in the setting of chemotherapy, suggesting that this may be a possible treatment strategy for NSCLC.

RESULTS

Human NSCLC tissues frequently have a fibrotic TME

To determine the impact of fibrosis on NSCLC, we first characterized the localization and relative abundance of reactive stroma within human NSCLC. To accomplish this, we performed histologic analysis of three patient cohorts with early-stage NSCLC, including two human tumor microarrays (TMAs) and one resection cohort from our institution (data file S1). To analyze reactive fibrosis, we first performed trichrome staining for collagen and immunohistochemical (IHC) analysis for α–smooth muscle actin (αSMA), a marker of activated fibroblasts, on NSCLC TMAs. We determined that the TME of NSCLC contains an increased amount of fibrosis compared with normal control lung tissue as defined by increased collagen deposition (Fig. 1, A and B, and fig. S1, A and B) and activated CAFs (Fig. 1, C and D). In addition, fibroblasts were often seen surrounding nests of tumor cells (Fig. 1C and fig. S1C). Given the sampling bias involved with procuring TMAs, we next used automated tissue analysis of hematoxylin and eosin (H&E)–stained sections from stages I and II, resected NSCLC samples obtained at our institution (Fig. 1, E and F, and data file S1). We determined that, on average, tumor-associated stroma comprised about 50% of the resection sample by area and ranged from 14.1 to 82.9% (Fig. 1G). These data suggest that most NSCLC harbors a substantial amount of tumor-associated fibrosis and desmoplasia.

To better understand how this tumor desmoplasia might relate to tumor immunity, we assessed T cell infiltrates. We performed CD8 and CK7 dual-IHC staining (fig. S1D) to determine $CD8^+$ T cell proximity to tumor cells and compared that with the amount of stroma from each sample. We found that the amount of stroma, whether calculated as stromal area or collagen density, correlated with reduced numbers of $CD8^+$ T cells within 50 μm of $CK7^+$ tumor cells (Fig. 1, H to J). These data suggest that increased tumor-associated fibrosis might affect T cell numbers in NSCLC.

Reactive fibrosis drives lung adenocarcinoma progression

To determine the role of fibrosis in tumor immune surveillance and tumor progression, we evaluated several mouse models of NSCLC for fibrosis. These included the commonly used genetically engineered mouse models (GEMMs) $Kras^{LSL\text{-}G12D}$;$Trp53^{fl/fl}$ (KPL) mice, who were given a single administration of intratracheal adenoviral-Cre recombinase to induce transformation (*44*). We also used orthotopic models of Lewis lung carcinoma (LLC) and a cell line derived from the lung of a *Trp53* heterozygous null, KPL GEMM, 9 months after intratracheal adenoviral-Cre recombinase administration (KPL86). In contrast to human NSCLC, across all these models, we found minimal collagen deposition [Fig. 2, A to C, phosphate-buffered saline (PBS)]. To model the impact reactive fibrosis that might have on tumor progression and immunity, we used two experimental systems. These included intratracheal administration of bleomycin (Bleo) or fluorescein isothiocyanate (FITC). Bleo induces alveolar epithelial cell injury, leading to increased free radicals and oxidative stress, which ultimately results in inflammation and reactive fibrosis within 2 to 4 weeks (*45*). FITC leads to increased alveolar and vascular damage, resulting in fibrosis in 2 to 3 weeks (*45*). To avoid potential immune-altering effects of prolonged exposure to either of these agents, we administered either a single dose of Bleo or FITC intratracheally 3 or 4 weeks before tissue collection for orthotopic models or GEMMs, respectively (Fig. 2). Administration of Bleo or FITC both increased collagen, as assessed by trichrome staining, deposition of both peritumorally and in the lung parenchyma, as well as tumor-associated αSMA^+ fibroblasts in all three models (Fig. 2, A to C, and fig. S2, A and B). Using flow cytometry, we observed increased numbers of $CD45^-$ $EpCAM^-$ $CD31^-$ CAFs in the setting of fibrosis (fig. S2C).

Induction of reactive fibrosis with either Bleo or FITC led to increased tumor progression in all models evaluated, including KPL GEMMs and orthotopic LLC and KPL86 models (Fig. 2, D to I, and fig. S2, D to F). Corresponding with promotion of tumor progression, we also saw more proliferation and less apoptosis in these tumors by Ki67 and cleaved caspase 3, respectively (fig. S2, G to I). In addition to increased tumor burden in fibrotic lungs,

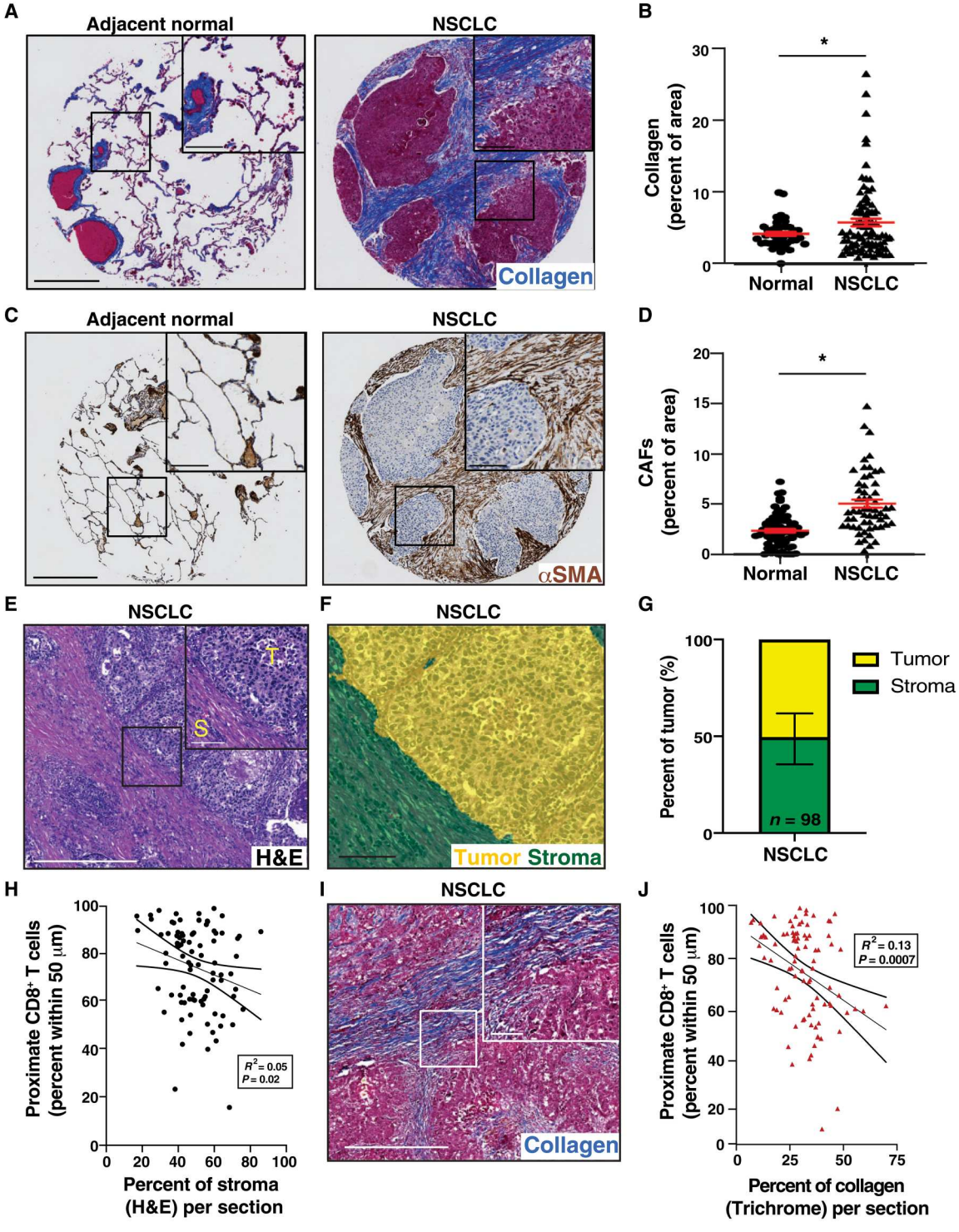

Fig. 1. Human NSCLC tissue harbors reactive fibrosis. (**A**) Shown are representative images from a TMA containing 75 early-stage lung adenocarcinomas with adjacent normal tissue stained with trichrome. Scale bars, 500 and 100 μm (inset). (**B**) Quantification of collagen content from (A). (**C**) Shown are representative images from a TMA containing 75 early-stage lung adenocarcinomas with adjacent normal tissue stained with αSMA. Scale bars, 500 and 100 μm (inset). (**D**) Quantification of collagen content from (C). (**E**) Shown is a representative H&E-stained section from resected NSCLC samples. Scale bars, 500 and 100 μm (inset). (**F**) Shown is a representative image from HALO analysis software for differentiating stroma area from tumor. Scale bar, 100 μm. (**G**) Quantification of tumor and stroma content in NSCLC samples shown in (E) and (F) ($n = 98$). (**H**) Shown is correlation analysis between proximal $CD8^+$ T cells and stroma content by H&E in NSCLC samples ($n = 98$). (**I**) Representative images from NSCLC sections stained with trichrome are shown. Scale bars, 500 and 100 μm (inset). (**J**) Shown is correlation analysis between proximal $CD8^+$ T cells and collagen content in trichrome-stained sections in NSCLC samples ($n = 98$). Data are presented as means ± SEM and were analyzed by two-sided *t* test between two groups or Pearson correlation and graphed using a linear regression model with 95% confidence intervals for (H) and (J). *$P < 0.05$.

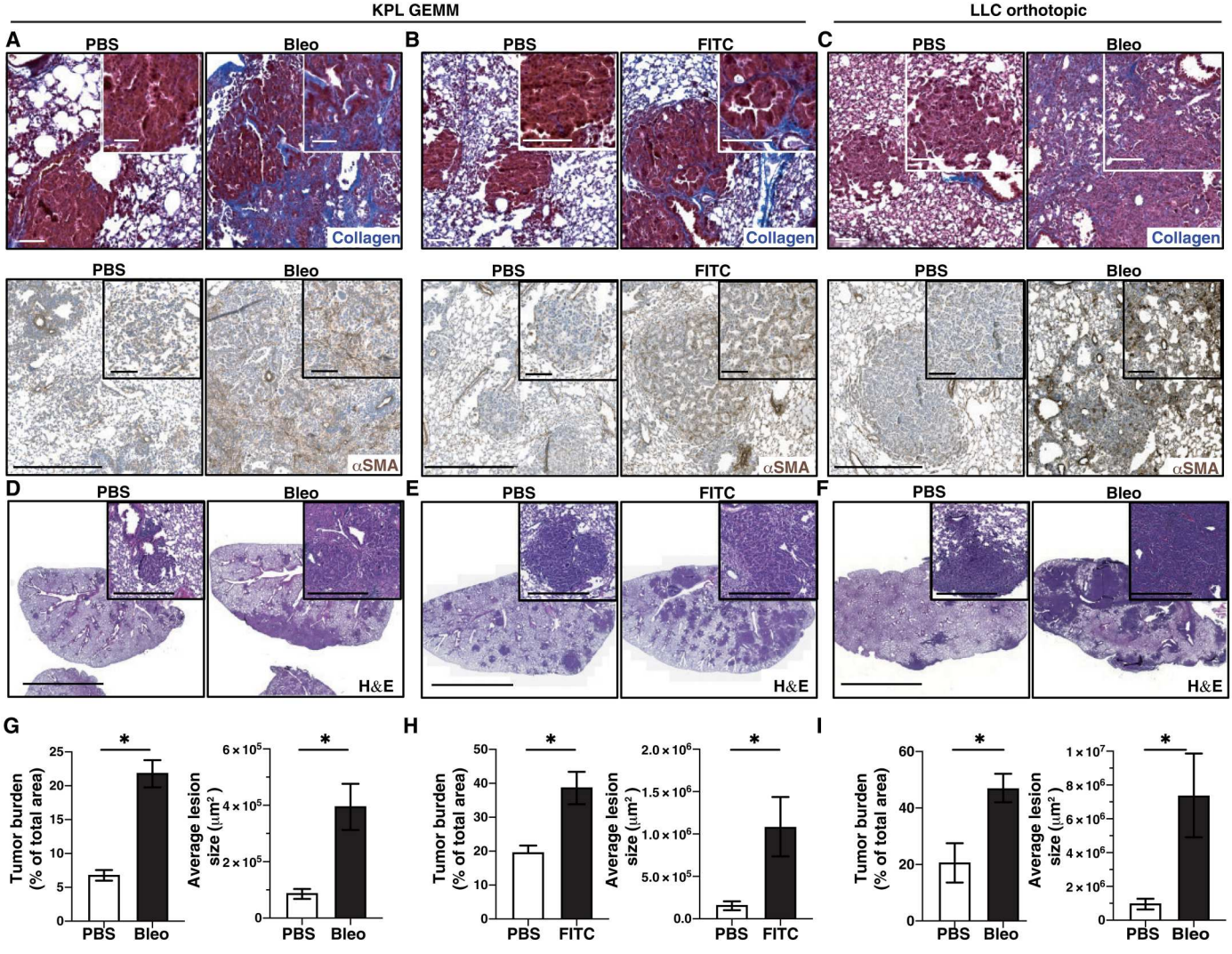

Fig. 2. Reactive fibrosis enhances cancer progression in mouse models of NSCLC. (**A** to **C**) Representative images are shown from trichrome-stained sections (top) or αSMA (bottom) from KPL GEMMs treated with PBS or Bleo (A) or FITC (B) or LLC orthotopic mice treated with PBS or Bleo (C). Scale bars, 100 μm. (**D** to **F**) Shown are representative H&E-stained sections from KPL GEMMs treated with PBS or Bleo (D) or FITC (E) or LLC orthotopic mice treated with PBS or Bleo (F). Scale bars, 5 mm and 100 μm (inset). (**G** to **I**) Quantification of tumor burden as a percentage of total lung area and average lesion size for tumors corresponding to (D) to (F), respectively ($n = 8$). Data are presented as means ± SEM and were analyzed by two-sided t test between two groups. *$P < 0.05$.

tumors from fibrotic lungs were more aggressive on the basis of a previously published grading system (fig. S2J) (*44*). Together, these data suggest that reactive fibrosis can be a strong driver of tumor progression.

Fibrosis impairs immune surveillance and T cell–mediated tumor control

Given the importance of T cell–mediated tumor control and our observation that fibrosis negatively correlated with T cells in human NSCLC, we sought to determine whether fibrosis impaired T cell immunity. Analysis of T cells by IHC showed reduced numbers of $CD8^+$ T cells within Bleo-induced fibrotic tumors from KPL GEMMs as well as LLC and KPL86 orthotopic models (Fig. 3, A to D, and fig. S3A). Similarly, reactive fibrosis induced by FITC also reduced the number of $CD8^+$ T cells within tumors from KPL GEMMs (fig. S3B). Analysis by flow cytometry found an increase in PD-1^+ $CD8^+$ T cells and $Foxp3^+$ $CD4^+$ T_{regs} in mice with fibrosis (fig. S3, C to E). To assess whether the effect of fibrosis on tumor control might be T cell mediated, $CD4^+$ and $CD8^+$ T cells were depleted in the presence or absence of Bleo in the orthotopic LLC model. In the absence of Bleo, we found that depletion of T cells led to an increase in tumor burden, indicating that T cells are able to restrain tumor growth in this model (Fig. 3E). In contrast, in the presence of Bleo, we found that depletion of T cells did not further increase tumor burden (Fig. 3E). These data suggest that fibrosis enhances tumor growth at least in part by impairing T cells.

To assess the impact of fibrosis on immune surveillance, we used KPL GEMMs that, under the control of Cre-recombinase, also express ovalbumin (OVA) fused to green fluorescent protein (GFP) (KPLOG) (Fig. 3F) (*29*). Within the resultant tumors, we observed a significant ($P = 0.02$) increase in $CD8^+$ T cells in KPLOG mice compared with KPL mice, suggesting an induction of T cell

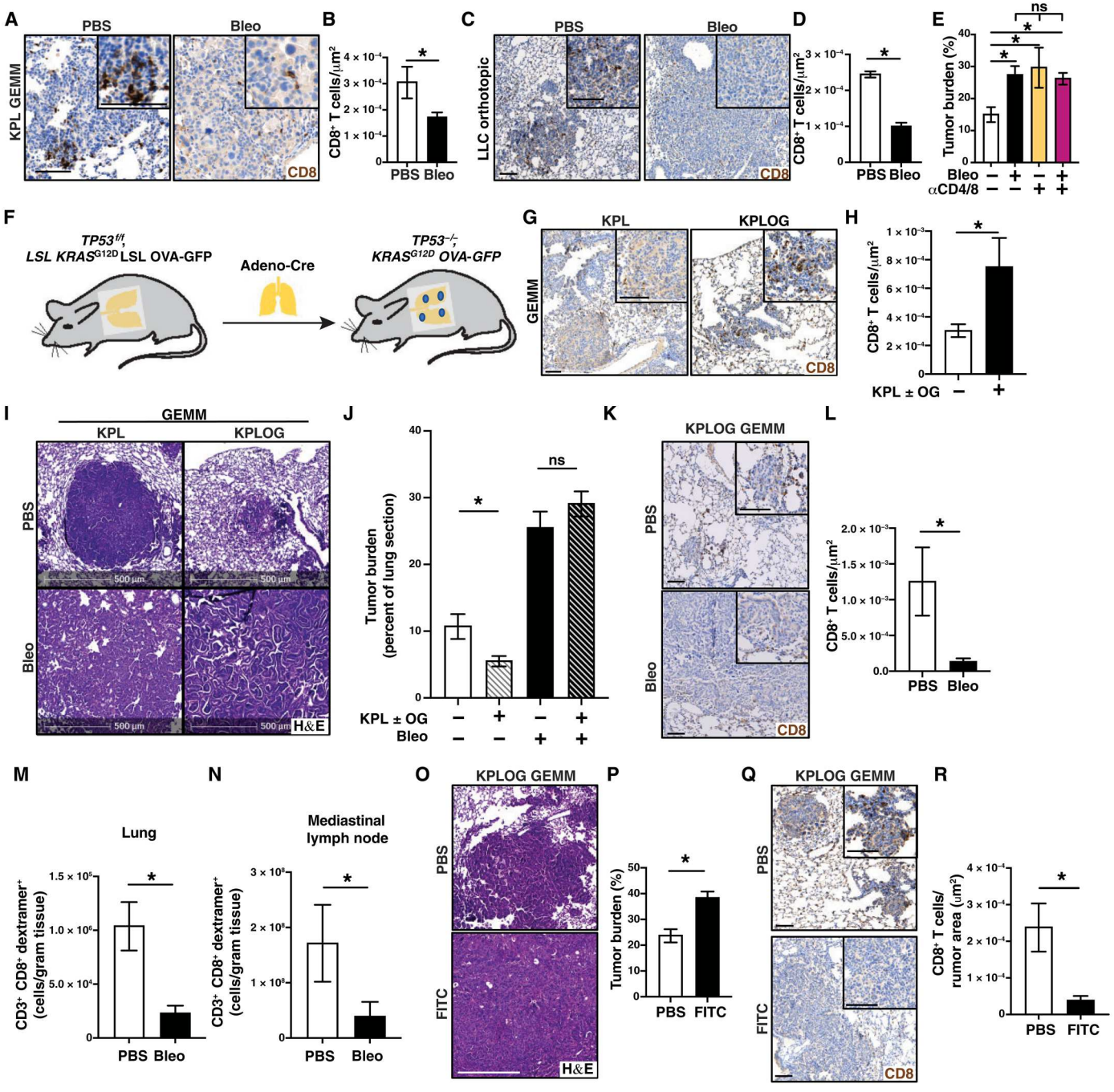

Fig. 3. Reactive fibrosis impairs immune surveillance in models of NSCLC. (**A** and **B**) Shown are representative images (A) of IHC-stained sections for CD8 and associated quantification (B) of $CD8^+$ T cells per tumor area in KPL GEMMs treated with PBS or Bleo ($n = 5$). (**C** and **D**) Shown are representative images (C) of IHC-stained sections for CD8 and associated quantification (D) of $CD8^+$ T cells per tumor area in LLC orthotopic mice with PBS or Bleo ($n = 3$). Scale bars, 50 μm (A and C). (**E**) Shown is quantification from LLC orthotopic mice treated with PBS or Bleo with or without depletion of CD4 and CD8 T cells. (**F**) Shown is a schematic of the KPL GEMM expressing ovalbumin (OVA)–GFP (KPLOG) tumor model. (**G** and **H**) Representative images from IHC-stained sections for CD8 (scale bar, 50 μm) (G) and associated quantification of $CD8^+$ T cells per tumor area (H) are shown for KPL or KPLOG GEMMs ($n = 5$). (**I**) Representative H&E-stained sections are shown from KPL or KPLOG GEMMs treated with PBS or Bleo. Scale bars, 500 μm. (**J**) Quantification of tumor burden in (I) ($n = 6$). (**K** and **L**) Representative images from IHC-stained sections for CD8 (K) and associated quantification of $CD8^+$ T cells per tumor area (L) in KPLOG GEMMs ($n = 5$). (**M** and **N**) Shown is quantification of OVA-specific, $CD8^+$ T cells in the lung (M) or draining lymph node (N) ($n = 6$). (**O** and **P**) Representative H&E-stained sections (O) and associated quantification of tumor burden (P) are shown for KPLOG GEMMs treated with PBS or FITC ($n = 8$). Scale bar, 500 μm. (**Q** and **R**) Shown are representative images from IHC-stained sections for CD8 (Q) and associated quantification of $CD8^+$ T cells per tumor area (R) in KPLOG GEMMs treated with PBS or FITC ($n = 5$). Data are presented as means ± SEM and were analyzed by two-sided *t* test between two groups or analysis of variance (E). $^*P < 0.05$. ns, not significant.

immunity (Fig. 3, G and H). Consistent with a role for immune surveillance in tumor control in this model (*29*), tumors derived from KPLOG mice expressing the OG antigen were smaller than their OG^- KPL littermates (Fig. 3, I and J). However, in the setting of fibrosis, the impact of the OG neoantigen expression on immune-mediated tumor control was abrogated, and both OG^+ and OG^- KPL mice had similarly accelerated tumor burdens (Fig. 3, I and J, and fig. S3F). These data demonstrate that fibrosis impairs neoantigen-driven, T cell–mediated tumor control. Consistent with our previous observations, fibrosis reduced the number of $CD8^+$ T cells present within the lungs and tumors of KPLOG mice (Fig. 3, K and L, and fig. S3G) while increasing forkhead box P3 $(Foxp3)^+$ T_{regs} (fig. S3, H and I). Flow cytometry for OVA-specific $dextramer^+$ T cells revealed reduced antigen-specific $CD8^+$ T cells in the fibrotic lungs (Fig. 3M) and in the draining lymph nodes of KPLOG GEMMs (Fig. 3N and fig. S3J). Together, these data suggest impaired T cell priming in the setting of fibrosis. We observed similar effects on tumor burden and $CD8^+$ T cell localization when fibrosis was induced with FITC, confirming that this is a fibrosis-mediated impairment of T cell–mediated tumor control and not a Bleo-specific effect on T cell function (Fig. 3, O to R, and fig. S3, K and L).

Fibrosis impairs checkpoint blockade efficacy in a model of NSCLC

Given the decreased antigen-specific T cells and immune surveillance we observed, we next sought to determine whether fibrosis would impair the efficacy of immune checkpoint blockade. To evaluate this, we evaluated tumor burden in KPL86 orthotopic tumor–bearing mice in various treatment settings. As above, the induction of fibrosis led to an increase in tumor burden (Fig. 4, A and B). Treatment with standard chemotherapy for NSCLC (carboplatin and pemetrexed) led to equivalent reductions in tumor burden regardless of the TME (Fig. 4, A and B). In the absence of a fibrotic TME, the addition of immune checkpoint blockade in the form of an anti–PD-1 antibody led to further reduction of tumor burden in the mice (Fig. 4, A and B). However, in the setting of fibrosis, checkpoint blockade had no additional benefit over chemotherapy, demonstrating that the fibrotic TME abrogates checkpoint blockade efficacy (Fig. 4, A and B). These data suggest that altered T cell immunity in the fibrotic TME limits the benefit of immune checkpoint blockade.

Lung fibrosis drives altered myeloid responses

To better understand how fibrosis might lead to an immunosuppressive TME, we first analyzed the tumor-infiltrating myeloid cells. In the lung, macrophages and conventional dendritic cells (cDCs) are the primary mediators of antigen presentation, and dysfunction in these cells leads to altered immune surveillance (*46*). Therefore, we evaluated the myeloid compartments from lungs of tumor-bearing mice with or without experimental fibrosis. In lung tumors from KPL GEMMs and LLC orthotopic models, we found that experimental fibrosis increased the number of total and $CD206^+$ macrophages but did not alter $Ly6G^+$ neutrophil numbers (Fig. 5, A and B, and fig. S4, A to D). To better characterize the localization of these macrophages, we performed IHC staining of F4/80, which revealed that experimental fibrosis induced increased macrophage infiltration both in the tumor nest and surrounding lung parenchyma (Fig. 5C). We next performed mass cytometry time of flight (CyTOF) analysis. In agreement with flow cytometry results, we observed increased CD206 expression on both interstitial and alveolar macrophages (Fig. 5, D to F). We also observed that both subsets of macrophages from the fibrotic lung TME expressed reduced major histocompatibility complex II (MHC-II) but increased MHC-I and PD-L1, suggesting an activated but potentially suppressive phenotype (Fig. 5, E and F). Together, these data suggest that the fibrotic lung TME not only leads to increased numbers of macrophages but also changes their phenotype.

We next evaluated lung macrophages by single-cell RNA sequencing (scRNA-seq). Uniform Manifold Approximation and Projection (UMAP) analysis identified several subpopulations of macrophages, including alveolar macrophages, interstitial macrophages, and proliferating macrophages (Fig. 5G). The most apparent transcriptional shift among these subsets was in alveolar macrophages (Fig. 5G). Consistent with prior data, alveolar macrophages in fibrotic lungs highly expressed *Mrc1* (CD206) and *Arg1* (arginase 1) (fig. S4, E and F). We next identified differentially expressed genes (DEGs) and performed gene set enrichment analysis

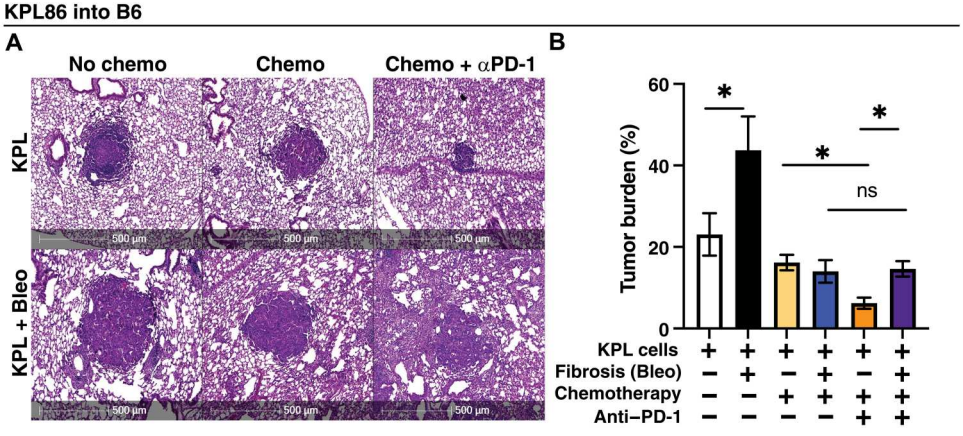

Fig. 4. Reactive fibrosis impairs response to immune checkpoint blockade. (**A**) Shown are representative H&E-stained lung sections from KPL86 orthotopic mice treated with vehicle, Chemo (carboplatin and pemetrexed), or Chemo combined with anti–PD-1 checkpoint blocking antibody. Scale bars, 500 μm. (**B**) Quantification of tumor burden from (A) (n = 8). Data are presented as means ± SEM and were analyzed by ANOVA. *P < 0.05.

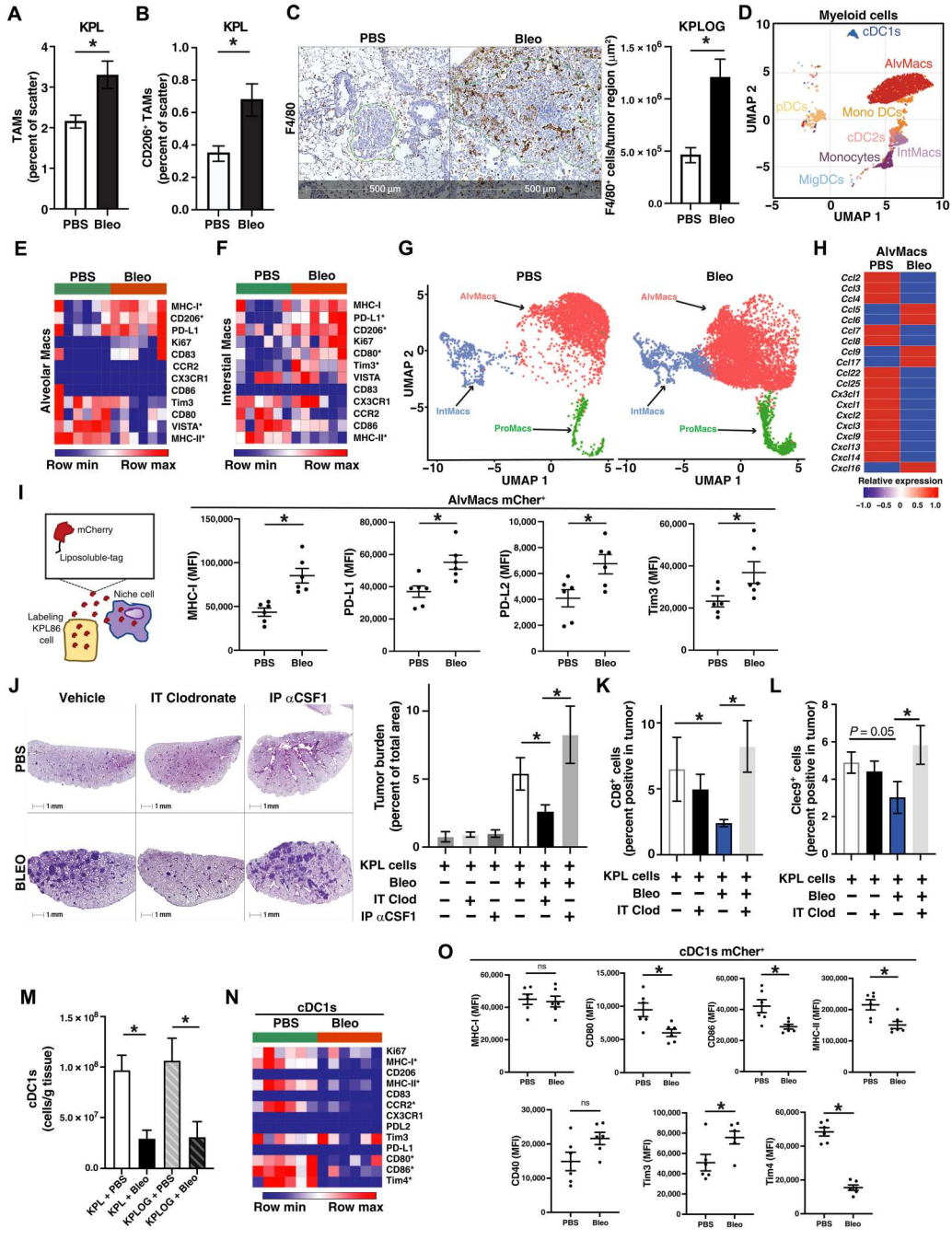

Fig. 5. Reactive fibrosis alters myeloid responses. (**A** and **B**) Shown is flow cytometry analysis measuring the frequency of tumor-associated macrophages (TAMs) (A) and CD206$^+$ TAMs (B) in KPL GEMMs treated with PBS or Bleo (n = 6). (**C**) Representative images from IHC-stained sections for F4/80 (scale bars, 500) and associated quantification of F4/80$^+$ TAMs per tumor area in KPLOG GEMMs (n = 6). (**D**) Shown is a UMAP projection depicting mass cytometry data for myeloid cells isolated from the lungs of PBS- or Bleo-treated KPLOG GEMMs. cDCs, conventional dendritic cells; AlvMacs, alveolar macrophages; pDCs, plasmacytoid dendritic cells; Mono DCs, monocytic dendritic cells; IntMacs, interstitial macrophages; MigDCs, migratory dendritic cells. (**E** and **F**) Heatmaps of selected targets on alveolar (E) and interstitial (F) macrophages are shown for the indicated treatment groups (n = 6). (**G**) Shown are UMAP projections of scRNA-seq data on macrophage subsets isolated from the lungs of KPLOG GEMMs treated with PBS or Bleo. ProMacs, proliferating macrophages. (**H**) Shown is a heatmap of statistically differentially expressed chemokine genes from alveolar macrophages isolated from the lungs of KPLOG GEMMs treated with PBS or Bleo. (**I**) Shown is a cartoon depicting the mCherry (mCher) system and flow cytometry analysis of mCher$^+$ alveolar macrophages from KPL86-bearing lungs treated with PBS or Bleo (n = 6). (**J** to **L**) Shown are representative H&E-stained lung sections from KPL86 orthotopic mice treated with IT clodronate or IP αCSF1 and associated quantification of tumor burden as a percentage of total lung area (n = 10) (J), quantification of CD8$^+$ T cells as a percentage of total cells (K), and quantification of Clec9α$^+$ cells as a percentage of total cells (L) from the designated cohorts (n = 10). (**M**) Shown is flow cytometry quantification of the frequency of cDC1s in lungs from KPL and KPLOG GEMMs (n = 6). (**N**) Shown is a heatmap of selected targets on cDC1s from mass cytometry of KPL GEMMs treated with PBS or Bleo (n = 6). (**O**) Shown is quantification of flow cytometry analysis of mCher$^+$ cDC1s from KPL86-bearing lungs treated with PBS or Bleo (n = 6). MFI, mean fluorescence intensity. Data are presented as means ± SEM and were analyzed by two-sided t test between two groups. *P < 0.05.

(GSEA). Consistent with residence in a fibrotic TME, we observed increases in integrin and SMAD2/3 signaling signatures in alveolar macrophages from Bleo-primed lungs (fig. S4G). We also found that alveolar macrophages in fibrotic lungs had reduced *Ccl3*, *Ccl4*, and *Cxcl9* expression but increased expression of *Ccl5*, *Ccl6*, *Ccl9*, and *Ccl17* (Fig. 5H and data file S2). Together, these data suggest that fibrosis leads to changes in macrophage phenotype that could affect cytotoxic T cell, T_{reg}, and cDC infiltration and function.

Because the traditional flow cytometry, CyTOF, and scRNA-seq approaches analyze the entire lung, including tumor and nontumor areas, we next sought to specifically interrogate tumor-interacting macrophages. To address this, we used KPL86 tumor cells expressing soluble mCherry (mCher$^+$). This system allows for the characterization of cells present within tumor nests, which will take up

mCher from their surroundings, and those not present in tumor nests will remain mCher negative (mCher$^-$) (Fig. 5I) (*47*). Using this system, we found that tumor-interacting alveolar macrophages from fibrotic lungs had increased expression of MHC-I, as well as PD-L1, PD-L2, and T cell immunoglobulin and mucin domain–containing-3 (Tim3) (Fig. 5I). These changes were not observed in mCher$^-$ alveolar macrophages (fig. S4H). Together, these data suggest that tumor-interacting macrophages may contribute to T cell dysfunction.

We next sought to determine the role of macrophage subsets in fibrosis-accelerated tumor progression. To deplete alveolar macrophages, we used intratracheal clodronate (IT clodronate) liposomes, and to deplete interstitial macrophages, we used intraperitoneal anti–colony stimulating factor 1 (CSF1) antibody (IP αCSF1). We observed a significant (P = 0.0001) reduction of alveolar macrophages, but not interstitial macrophages, in mice treated with IT clodronate, whereas IP αCSF1 had no effect on alveolar macrophages but significantly (P < 0.00001) reduced the numbers of interstitial macrophages (fig. S4, I and J). Depletion of alveolar macrophages, but not interstitial macrophages, led to a significant (P = 0.01) reduction in the tumor burden in fibrotic lungs but did not affect tumor progression in the absence of experimental fibrosis (Fig. 5J). Paralleling changes in tumor progression, depletion of alveolar macrophages restored CD8$^+$ T cell and Clec9a$^+$ cDC infiltration, comparable to the nonfibrotic lung (Fig. 5, K and L). These data suggest that fibrosis-induced changes in alveolar macrophages are specifically important in driving tumor progression and repressing tumor immunity.

Given the role cDCs play in priming the antitumor immune response, we further characterized them. In KPL GEMMs, we observed a reduction in both CD103$^+$ cDC1s and CD11b$^+$ cDC2s in the lung TME of mice primed with Bleo (Fig. 5M and fig. S4, K and L). Characterization by CyTOF revealed reduced expression of MHC-I and MHC-II and the costimulatory molecules CD80 and CD86 in cDC1s (Fig. 5N). We also found similar changes in cDC2s (fig. S4M). scRNA-seq analysis revealed reduced Toll-like receptors, interleukin-6 (IL-6), IL-12, and CD40 signaling pathway signatures in cDC1s from the fibrotic lung (fig. S4, N and O). These cells also exhibited reduced allograft rejection and inflammatory response (fig. S4O). We next characterized tumor-interacting and nontumor-interacting cDCs using the soluble mCher system. We found that experimental fibrosis led to decreased expression of MHC-II, CD80, and CD86 on mCher$^+$ cDC1, whereas these did not change in mCher$^-$ cDC1s (Fig. 5O and fig. S4P). Expression of the immune checkpoint Tim3 was increased, whereas Tim4, which is involved in antigen uptake (*48*), was reduced on mCher$^+$ cDC1s in fibrotic lung tumors (Fig. 5O). Together, these data suggest that fibrosis impairs cDC1 infiltration into the TME and may impair cDC1 function within the lung tumors.

Altered fibroblast phenotypes contribute to the immunosuppressive TME in NSCLC

We previously observed increased numbers of CAFs in NSCLC compared with healthy tissue. To further characterize these cells, we analyzed the lungs of mice treated with PBS or Bleo by flow cytometry and again saw an increased number of CD45$^-$ EpCAM$^-$ CD31$^-$ CAFs in the fibrotic lung (Fig. 6A and fig. S5A). When we analyzed markers of specific CAFs, we found that fibroblast activation protein α (FAP$^+$) and CD90$^+$ (Thy-1) CAFs increased in the fibrotic lung (Fig. 6, B and C, and fig. S5, B to D). CD90$^+$ and FAP$^+$ CAFs have been associated with reduced survival in patients with NSCLC (*49*, *50*). Together, these data show that total CAFs increase in these models of lung cancer–associated fibrosis, but there is some specificity to which CAF phenotypes are altered.

Recently, the heterogeneity of CAFs within NSCLC has been better elucidated using scRNA-seq (*42*). To better understand the molecular and functional heterogeneity of CAFs in our fibrotic tumor models, we isolated CD45$^-$ EpCAM$^-$ CD31$^-$ cells from KPL GEMM tumor-bearing mice with and without Bleo treatment and performed scRNA-seq. UMAP analysis of CAFs revealed 10 clusters that all express key identifying genes such as *Col1a1* (fig. S5, E and F, and data file S3). Xie *et al.* (*51*) demonstrated three primary populations of fibroblasts within the lung separated by expression of αSMA (*Acta2*), collagen 13 (*Col13a1*), and collagen 14 (*Col14a1*). We analyzed the 10 clusters for these markers to group them into three distinct clusters. *Acta2*-expressing [myofibroblasts (Myofib)], *Col14a1*-expressing (Col14), and *Col13a1*-expressing (Col13) fibroblasts were identified within lung mesenchymal cells (Fig. 6D, fig. S5G, and data file S3). Comparing PBS-treated with Bleo-treated tumor–bearing lungs revealed a relative increase in Col13$^+$ fibroblasts and Myofib with a concomitant decrease in Col14$^+$ fibroblasts (Fig. 6E) and a transcriptional shift in the Col13$^+$ fibroblasts (Fig. 6F). Specific subsets of fibroblasts may play a role in promoting immune suppression within the TME (*28*–*30*). Given the alterations observed in the Col13 fibroblast population after inducing fibrosis, we focused on this population and asked whether they exhibited an altered chemokine or cytokine profile that might affect the TME immune composition. Differential gene expression analysis found the up-regulation of *Ccl6*, *Cxcl12*, and *Cxcl16* in fibroblasts that have previously been associated with Bleo-induced lung fibrosis (Fig. 6G and data file S4) (*52*, *53*). We also identified changes in several chemokines, suggesting that fibrosis induced an immunosuppressive microenvironment. For example, consistent with the observed alterations in macrophages and T_{regs}, we noted increases in chemokines associated with tissue infiltration of myeloid cells (*Ccl4* and *Ccl9*) (*54*, *55*) and T_{reg} recruitment (*Cxcl12*) (Fig. 6G and data file S4) (*56*, *57*). *Ccl19*, a chemoattractant for cDC infiltration, was reduced in Col13 fibroblasts isolated from fibrotic lungs (*58*, *59*). Chemokines involved in the recruitment of cytotoxic T cells, such as *Cxcl10* (*60*, *61*), were reduced in the fibrotic model, suggesting that the changes in CAFs may lead to immunosuppression (Fig. 6G and data file S4).

We next sought to test whether fibroblasts from Bleo-induced fibrotic lungs could modulate macrophage phenotype. To accomplish this, we cocultured primary fibroblasts from control or Bleo-exposed lungs with bone marrow–derived macrophages (BMDMs) using a Transwell system. We found that compared with controls, fibroblasts from fibrotic lungs induced higher expression of *Arg1*, *Mrc1* (CD206), and *Il6* (fig. S5, H to J). These data suggest that activated fibroblasts from fibrotic lungs may contribute to immune suppression through regulation of macrophages.

To test the impact of activated fibroblasts in vivo, we used genetic depletion of platelet-derived growth factor receptor α$^+$ (PDGFRα$^+$) cells because PDGFRα$^+$ is expressed by both Col13$^+$ and Col14$^+$ fibroblasts but not αSMA$^+$ fibroblasts (fig. S5K). Crossing *Pdgfra*$^{tm1.1(cre/ERT2)}$(PDGFRα-CreER^{T2}) mice (*62*) to lox-stop-lox (LSL)–diphtheria toxin receptor (DTR) mice (*63*) enabled the inducible expression of DTR on PDGFRα$^+$ cells in the resultant

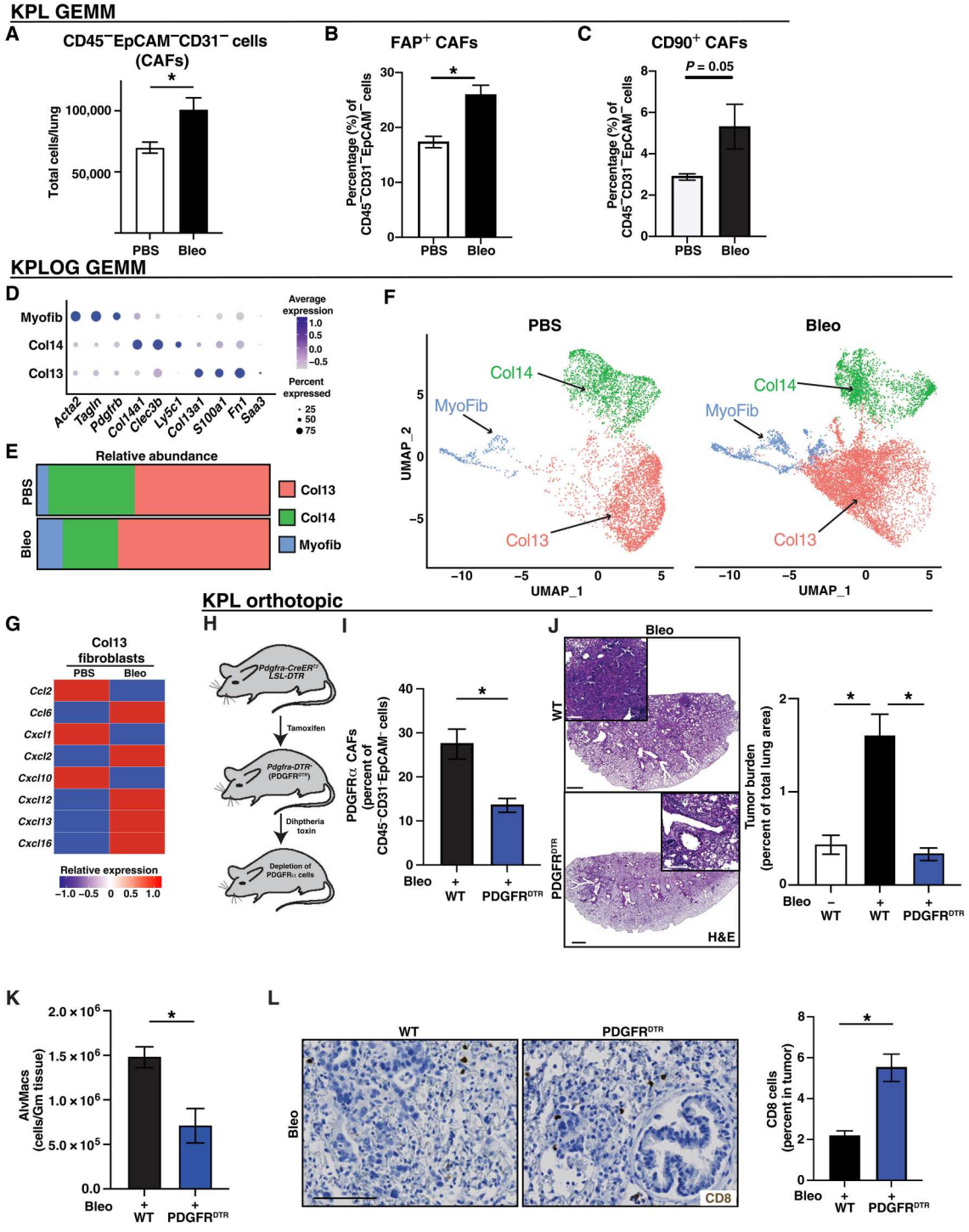

Fig. 6. Phenotypic changes in CAFs alter immune cell recruitment in the fibrotic TME and enhance TGFβ expression. (**A** to **C**) Shown is flow cytometry analysis of total CD45⁻ EpCAM⁻ CD31⁻ cancer-associated fibroblasts (CAFs) (A), FAP⁺ CAFs (B), and CD90⁺ CAFs (C) from the lungs of KPL GEMMs treated with PBS or Bleo ($n = 6$). (**D**) The dotplot shows selected markers of myofibroblasts (Myofib), Col14, and Col13 CAFs. (**E**) Shown is the relative abundance of each CAF subset in the lungs of KPLOG GEMMs treated with PBS or Bleo. (**F**) Shown are UMAP projections of scRNA-seq data for Myofib, Col14, and Col13 CAFs from the lungs of PBS- and Bleo-treated KPLOG GEMMs. (**G**) The heatmap shows chemokine genes with significantly altered expression in Col13 CAFs. (**H**) Shown is the schema for generation of PDGFRα-cell depletion by crossing Pdgfra-CreER^{T2} mice with LSL-DTR mice (PDGFR^{DTR}). (**I**) Shown is flow cytometry analysis of PDGFRα CAFs after PDGFRα depletion. (**J**) Shown are representative H&E-stained sections from KPL86-bearing lungs of PDGFR^{DTR} or littermate controls (WT) treated with Bleo [scale bars, 1 mm and 100 μm (inset)] and quantification of tumor burden from PDGFR^{DTR} or littermate controls (WT) treated with PBS or Bleo. (**K**) Shown is flow cytometry quantification of alveolar macrophages after PDGFRα depletion. (**L**) Shown are representative images from IHC-stained sections for CD8 and associated quantification of CD8⁺ T cells as a percentage of cells in the tumor area in PDGFR^{DTR} or littermate controls (WT) treated with Bleo ($n = 7$). Data are presented as means ± SEM and were analyzed by two-sided t test between two groups.*$P < 0.05$.

mice (PDGFRα^{DTR}). Tamoxifen administered for five consecutive days followed by a single dose of diphtheria toxin resulted in efficient depletion of PDGFRα cells, whereas no change in αSMA cells was observed (Fig. 6, H and I, and fig. S5, L and M). After depletion of PDGFRα$^+$ cells, including Col13$^+$ fibroblasts, tumor burden was markedly reduced in mice treated with Bleo (Fig. 6J). Flow cytometry revealed a reduction in alveolar macrophages (Fig. 6K) and an increase in intratumoral CD8$^+$ T cell numbers (Fig. 6L). This suggests that PDGFRα$^+$ fibroblasts, which include Col13$^+$ fibroblasts, play a role in altered immune infiltration in lung tumors in the setting of fibrosis. Consistent with what is known about Bleo-induced pulmonary fibrosis, overrepresentation analysis found that the TGFβ response pathway was increased in Bleo-treated compared with PBS-treated Col13$^+$ fibroblasts (fig. S5N). Although nearly all CAF subsets had cells that expressed the TGFβ response signature (data file S5), Col13$^+$ fibroblasts had a large positive signal, suggesting that this was the dominant CAF subset expressing TGFβ (fig. S5O). We confirmed increased TGFβ within the Bleo-treated lungs using IHC (fig. S5P). Together, these data suggest that in addition to driving an increase in specific CAF subsets, fibrosis shifts their phenotype toward being more immunosuppressive.

Targeting transforming growth factor β receptor-1 (TGFβR-I) signaling restores immune checkpoint efficacy only when combined with chemotherapy

TGFβ is well established in the pathogenesis of pulmonary fibrosis (*64*, *65*), and we confirmed that TGFβ expression in the lung, using intratracheal delivery of adeno-associated virus (AAV) serotype 6 expressing TGFβ1, could induce fibrosis as measured by collagen deposition (fig. S6A). Furthermore, lung AAV-TGFβ1 expression led to increased tumor burden and CD206 macrophage infiltration and reduced intratumor CD8$^+$ T cells (fig. S6, A to D) comparable to Bleo- or FITC-induced experimental fibrosis models. We next sought to determine whether we could reverse the protumorigenic phenotype of pulmonary fibrosis observed in our models. To this end, we evaluated several agents that are currently used to treat pulmonary fibrosis in humans, including nintedanib and pirfenidone. However, these agents failed to alter the amount of collagen 1 deposition when given after the establishment of tumor-associated fibrosis (Fig. 7A and fig. S6E). Because we had observed that increased TGFβ signaling response in the Bleo-exposed fibroblasts and TGFβ overexpression in the lung recapitulated the phenotype observed in the fibrotic lungs treated with Bleo or FITC, we sought to target this pathway using a tool compound TGFβR-I inhibitor, Ly364947. We found that Ly364947 was able to mostly reduce the amount of collagen I within the lung when given after induction of fibrosis (Fig. 7A and fig. S6E). Furthermore, whereas fibrosis significantly (P = 0.017) reduced the number of CD8$^+$ T cells, treatment with Ly364947 restored pulmonary CD8$^+$ T cell numbers back to baseline (Fig. 7B). By contrast, nintedanib and pirfenidone had similar frequencies of CD8$^+$ T cells as the fibrotic lung alone (Fig. 7B). Consistent with this finding, treatment of tumor-bearing mice with Ly364947 had a modest effect on tumor burden in the fibrotic lung compared with vehicle control–, nintedanib-, or pirfenidone-treated mice (Fig. 7C).

To determine whether the TGFβR-I inhibitor Ly364947 was able to synergize with standard-of-care treatments for NSCLC, we treated mice with fibrotic, tumor-bearing lungs with the following treatment regimens: Ly364947 alone, Ly364947 combined with an anti–PD-1 immunoglobulin G (IgG) (PD-1), carboplatin plus pemetrexed combined with PD-1 (Chemo/PD-1), or Chemo/PD-1 plus Ly364947. Treatment with Ly364947 alone led to a slight decrease in tumor burden (Fig. 7, D and E). Combining Ly364947 with either PD-1 or Chemo alone failed to improve tumor burden compared with vehicle control (Fig. 7, D and E, and fig. S6F). Chemo/PD-1 significantly (P = 0.0002) reduced tumor burden compared with controls (Fig. 7, D and E). However, combining Chemo/PD-1 with Ly364947 led to a reduction in tumor burden to near-baseline (without fibrosis) and restored tumor-infiltrating CD8$^+$ T cells, suggesting that the addition of Ly364947 enhances the efficacy of Chemo/PD-1 (Fig. 7, D and E, and fig. S6G), a standard treatment approach for patients with NSCLC. We only observed a benefit from adding TGFβR1 inhibition to Chemo/PD-1 on tumor burden and CD8$^+$ T cell and Clec9α$^+$ cDC1 infiltration in the presence of experimental fibrosis, suggesting that in the absence of fibrosis-associated TGFβ, signaling may not have reached a critical threshold (Fig. 7, F to H). To explore the utility of these findings in human samples, we analyzed data from POPLAR and OAK clinical trials using atezolizumab in patients with metastatic NSCLC (*66*). We found that the TGFβ response signature that we observed in the Col13$^+$ CAFs correlated with improved overall survival in these patients (Fig. 7I and fig. S6H). Furthermore, a gene signature of the top 50 genes from Col13 CAFs (data file S3) correlated with increased M2 macrophages (Fig. 7J) but reduced M1 macrophages (Fig. 7K), activated dendritic cells (Fig. 7L), and CD8$^+$ T cells (fig. S6I). Together, these data suggest that these TME elements could be important in patients receiving immune checkpoint blockade.

DISCUSSION

Our data demonstrated that fibrosis in NSCLC leads to lung tumor progression and T cell dysfunction. The fibrotic TME led to changes in innate immunity and reduced numbers of cDCs, with the remaining cDC1s appearing to be more tolerant. In contrast, we observed increased macrophage populations indicative of an immunosuppressive phenotype. We also identified distinct changes within the Col13$^+$ CAF subsets, suggesting that these cells produce chemokines to recruit macrophages and T_{regs} and not recruit cDCs and cytotoxic T cells in the setting of fibrosis. Furthermore, coculture of fibroblasts from fibrotic lungs led to increased expression of several genes associated with immunosuppressive macrophages. Targeting fibrosis through TGFβR-I signaling led to enhanced infiltration of T cells and improved response to combined immune checkpoint blockade and chemotherapy but only in the setting of fibrosis, suggesting that the benefit is directly related to fibrosis.

Fibrosis has been identified as a key modulator of neoplastic progression in multiple cancer types (*67*). Fibrosis is composed of a dense ECM and fibroblasts. Multiple studies have demonstrated the importance of fibrosis in modulating immune surveillance (*28*–*30*). Most patients with NSCLC have a smoking history, and this is associated with fibrotic remodeling and scarring of lung tissue (*39*). Furthermore, conditions with increased pulmonary fibrosis, such as idiopathic pulmonary fibrosis, are associated with increased incidence of lung cancer; likewise, patients with early-stage NSCLC who harbor higher amounts of cancer-associated fibrosis have a shorter life expectancy (*36*–*38*, *40*). Although fibrosis

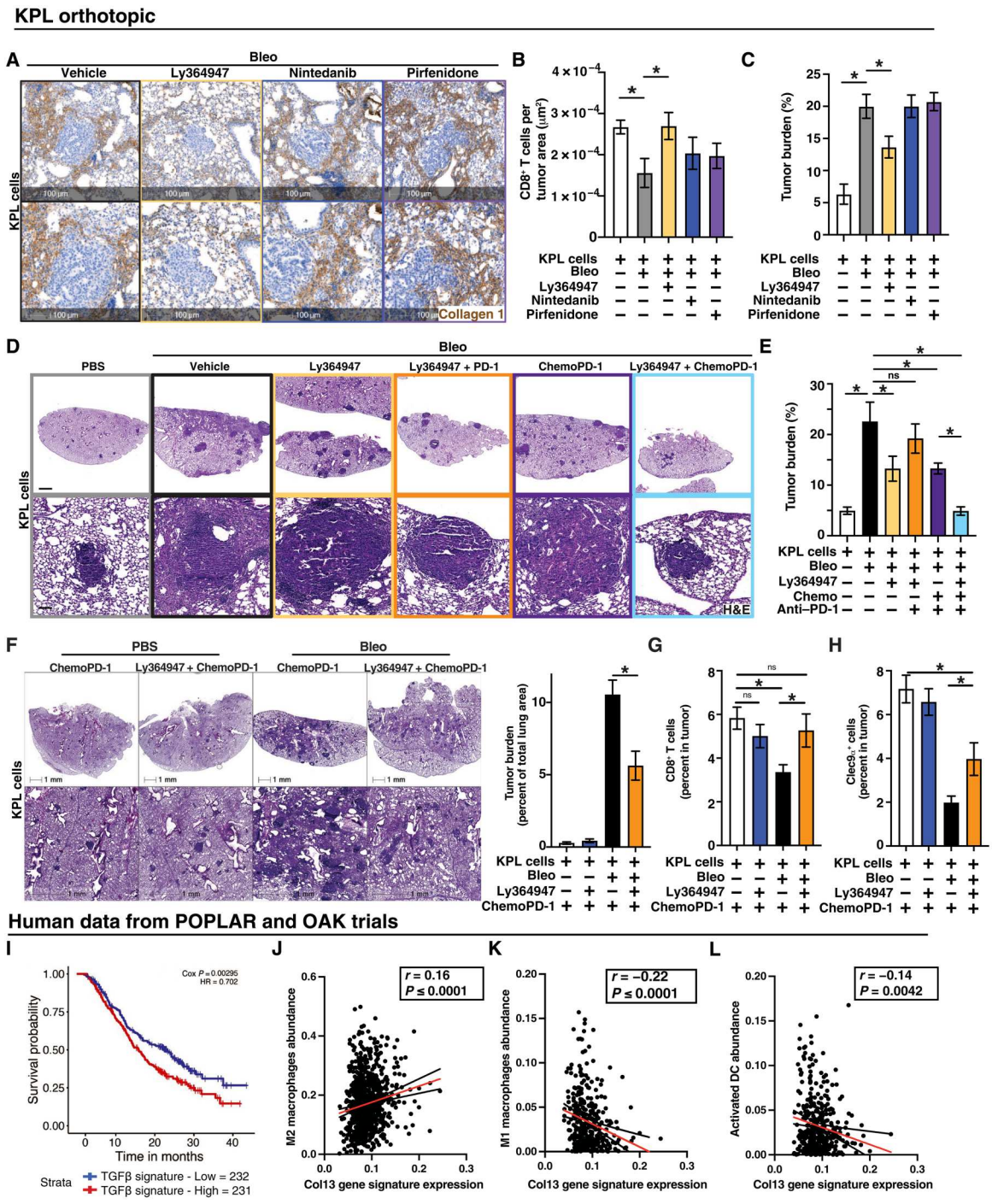

Fig. 7. Targeting TGFβR-I signaling enhances efficacy of chemotherapy combined with checkpoint blockade. (**A**) Shown are representative images of IHC-stained for collagen I in lung tissue in KPL86 orthotopic tumor–bearing mice treated as indicated. (**B**) Quantification of lung tumors IHC-stained for $CD8^+$ T cells in KPL86 orthotopic tumor–bearing mice treated as indicated ($n = 8$). (**C**) Quantification of tumor burden in KPL86 orthotopic tumor–bearing mice treated as indicated ($n = 8$). (**D**) Shown are representative H&E-stained lung sections from KPL86 orthotopic tumor–bearing mice treated with vehicle, Ly364947, Ly364947, and anti–PD-1, Chemo (carboplatin and pemetrexed) combined with anti–PD-1 checkpoint blocking antibody (Chemo/PD-1), or Ly364947 combined with Chemo/PD-1. Scale bars, 1 mm (top) and 100 μm (bottom). (**E**) Quantification of tumor burden from (D) ($n = 8$). (**F**) Shown are representative H&E-stained lung sections from KPL86 orthotopic tumor–bearing mice treated with Chemo (carboplatin and pemetrexed) combined with anti–PD-1 checkpoint–blocking antibody (Chemo/PD-1) or Ly364947 combined with Chemo/PD-1 (scale bars, 1 mm) with quantification of tumor burden ($n = 10$). (**G** and **H**) Quantification of $CD8^+$ T cells (G) and $Clec9\alpha^+$ cDC1s (H) measured by IHC is shown for lung tissue isolated from KPL86 orthotopic tumor–bearing mice from (F) ($n = 10$). (**I**) Shown is a Kaplan-Meyer curve for patients with low or high expression of a TGFβ signature from the POPLAR and OAK clinical trials (HR, hazard ratio). (**J** to **L**) Shown are correlation analyses between a Col13 gene signature and CIBERSORT clusters of M2_Macrophages (J), M1_Macrophages (K), and activated DCs (L). Data are presented as means ± SEM and were analyzed by two-sided *t* test between two groups, ANOVA, Cox regression for Kaplan-Meier survival curve (I), or Pearson correlation (J to L) . $^*P < 0.05$.

has been associated with poor prognosis for patients with NSCLC (*36*, *37*), its impact on immune surveillance and response to immunotherapy has remained poorly understood. Our initial evaluation of patient-derived surgical resection samples shows that patients with NSCLC often have a robust fibrotic TME. The degree of fibrosis correlated with reduced T cell infiltration, which has previously been associated with improved overall survival (*68*). We then sought to determine the role of fibrosis in immune surveillance of NSCLC and developed several models to study this in vivo. In animal models, we showed that experimentally induced lung fibrosis enhanced lung tumor progression. Although the methods are different, these findings are consistent with a recent study evaluating the role of radiation-induced fibrosis and posttreatment progression (*69*). We also observed decreased T cell infiltration in animal models of tumor-associated fibrosis, similar to the findings observed in human NSCLC. Consistent with fibrosis-related reduction of T cell infiltration playing a prominent role in tumor progression, depletion of T cells in the presence of fibrosis failed to elicit disease progression beyond that of fibrosis alone.

T cell–mediated tumor control requires activation of antigen-specific T cells, which most commonly occurs through cDCs that present antigen within the draining lymph node. These T cells are then recruited back to the TME through signaling chemokines such as CXCL9 and CXCL10 (*14*, *19*). We observed reduced T cell infiltration into the fibrotic lung and determined that, within the fibrotic lung microenvironment, cDCs were reduced. This is consistent with previous data that demonstrate a need for dendritic cells to be able to properly prime an antigen-specific immune response (*29*). In particular, $CD103^+$ cDC1s, which are critical regulators of the antitumor immune response, including T cell infiltration (*18*), were reduced. The dendritic cells that were present exhibited reduced antigen presentation machinery and CCR2, which has been shown to be critical for the migration of dendritic cells within the lung (*70*). By analyzing the macrophage populations, we identified an increase in the number of $CD206^+$ macrophages and an increase in arginase 1 ($ARG1^+$) alveolar macrophages, both of which are associated with an immunosuppressive TME (*71*–*73*). Despite an increase in interferon responses, we found reduced inflammatory response and allograft rejection pathways, suggesting a dysfunctional tissue repair cascade that results in impaired immune cell priming. Depletion of alveolar macrophages led to a rescue of both T cell infiltration and improved tumor burden in the fibrotic lung.

CAFs are a critical component of tumor stroma. In addition to producing much of the tumor ECM, they can also play a critical role modulating immune surveillance either through direct immune cell sequestration or recruitment of various immune cells by chemokines (*74*–*76*). We identified a shift in the several populations of CAFs, including increases in Myofib and $Col13^+$ CAFs. Not only were these two populations proportionally increased in the fibrotic TME but also their chemokine profile suggested that they were more likely to recruit tumor-promoting macrophages and T_{regs} while reducing recruitment of cDCs and cytotoxic T cells. Coculture of fibroblasts with BMDMs led to similar increases in genes associated with an immunosuppressive macrophage. Furthermore, depletion of PDGFRα cells led to reduced tumor burden and improvement in $CD8^+$ T cell infiltration. CAFs are known to be a source of TGFβ, and both $Col13^+$ CAFs and Myofib had a TGFβ-responsive signature in our lung model. TGFβ signaling can impair tumor immune surveillance (*77*, *78*). Despite promising preclinical data suggesting that targeting TGFβ signaling would lead to tumor responses, multiple trials have failed to demonstrate a meaningful clinical benefit of targeting TGFβ signaling, either targeting TGFβ or TGFβR-I, when combined with immune checkpoint blockade in NSCLC (NCT03631706 and NCT02423343). Consistent with these clinical observations, targeting TGFβR-I signaling either alone or in combination with immune checkpoint blockade had minimal benefit in our NSCLC models, despite reducing fibrosis and improving T cell infiltration. However, we saw that the addition of chemotherapy enhanced the benefit of TGFβR-I inhibition and immune checkpoint blockade. Why TGFβ-targeting agents have failed to provide clinical benefit when added to immune checkpoint blockade is unknown; however, recent data suggest that one possible mechanism is that chemotherapy can also play an important immune-modulating role and either enhance or impair immune checkpoint efficacy that improves antitumor immunity by reducing immunosuppressive cells (*79*–*82*). We found that combining TGFβR-I inhibition and immune checkpoint blockade with chemotherapy increased efficacy in our fibrotic NSCLC models, suggesting that this may be a potential strategy for treating human NSCLC.

Our study has the following limitations. The human data represent correlation, not causation, and require further study in a more prospective manner. Our mouse models use experimental induction of pulmonary fibrosis. Although we used several different types of experimental systems, none of these models of fibrosis can fully recapitulate the fibrosis observed in patients with NSCLC. Human causes of fibrosis in NSCLC likely include prolonged exposure to cigarette smoke, underlying genetics of NSCLC, and additional environmental factors that have not been modeled here. Additional studies are needed to determine the optimal way in which to target fibrosis in patients.

Together, these data suggest that, in NSCLC, fibrosis leads to tumor progression through reduced antitumor immunity. Fibrosis induces alterations in fibroblasts and tumor-associated macrophages that impaired dendritic cells and T cell responses, which ultimately reduced the antitumor immune responses necessary for optimal checkpoint therapy efficacy. Thus, treatment strategies targeting this fibrotic TME could improve responses to chemotherapy and immunotherapy in human NSCLC.

MATERIALS AND METHODS

Study design

This study was designed to understand the impact of fibrosis on immune surveillance and response to immune checkpoint blockade in NSCLC. We used two well-established pulmonary fibrosis models to evaluate the impact of fibrosis on NSCLC progression in murine models of NSCLC. We used conventional histology and IHC approaches along with flow cytometry, mass CyTOF, and scRNA-seq. Historical human NSCLC tissue blocks were obtained at Washington University and the Siteman Cancer Center under Institutional Review Board protocol nos. 201908148 and 201805041. All animal studies were approved by the Washington University School of Medicine Institutional Animal Studies Committee. The investigators were not blinded to the treatment conditions. Sample sizes are given in the respective figure legends and were calculated to achieve a minimum power of 95%.

Murine models

KPL or KPLOG mice were generated by delivering adenovirus Cre-recombinase into the tracheas of KP (*Kras*$^{LSL\text{-}G12D}$;*Trp53*$^{fl/fl}$) or KPOG (*Kras*$^{LSL\text{-}G12D}$;*Trp53*$^{fl/fl}$ *OVA-GFP*) mice (*29*). *Pdgfa*^{ERT2}-DTR^{+} (PDFGR^{DTR}) mice were generated by crossing B6.129S-*Pdgfra*$^{tm1.1(cre/ERT2)}$ (strain: 032770, the Jackson Laboratory, Maine) with C57BL/6-*Gt*(*ROSA*)*26Sor*$^{tm1(HBEGF)Awai}$/J mice [strain: 007900; ROSA26iDTR (LSL-DTR), the Jackson Laboratory]. All mice used in these studies have been bred to the C57BL/6J background in our laboratory using speed congenics and further backcrossed more than five times. All mice were housed, bred, and maintained under specific pathogen–free conditions in accordance with National Institutes of Health–Association for Assessment and Accreditation of Laboratory Animal Care International (AAALAC) standards and were consistent with the Washington University School of Medicine Institutional Animal Care and Use Committee regulations (protocol nos. 20160265 and 19-0856).

The KPL86 cell line was derived from lung tissues of the 9-month-old *Kras*$^{LSL\text{-}G12D}$/*p53*$^{flox/+}$ female mouse treated with adenovirus-delivered Cre-recombinase (University of Iowa Viral Vector Core). Cells were grown on collagen-coated tissue culture flasks for <10 passages. The KPL-mCher cell line was generated using the KPL86 cell line as previously described (*47*). To establish orthotopic NSCLC models, 500,000 KPL86, KPL-mCher, or LLC cells in 100 μl of PBS (Trevigen) were retro-orbitally injected into 8- to 12-week-old C57BL/6 mice.

A single dose of Bleo (1 mg/kg), FITC (3.5 mg/kg), or PBS was intratracheally administered in anesthetized (ketamine/xylazine cocktail) and intubated mice 2 days after the establishment of orthotopic models to avoid altering seeding of the cancer cell lines. Mice were randomized after the administration of the fibrosis-inducing agent. Mice were euthanized at 3 weeks after the introduction of cancer cells into the mice. In GEMMs, Bleo or FITC was administered 4 weeks after the administration of adenovirus Cre-recombinase and at least 4 weeks before end points to allow for ample time for fibrosis to develop and limit the direct effect of these agents on the immune cells within the lung at the time of euthanasia.

Macrophage depletion studies

To deplete pulmonary macrophages, 6- to 8-week-old C57BL/6J mice were treated with three doses of CSF1-neutralizing antibody (clone 5A1, Bio X Cell) (1, 0.5, and 0.5 mg on days −2, 0, and 7; Fig. 5, K and M) and three doses of clodronate-containing liposomes (200 μl each on days −2 and 5; Liposoma). Control mice were treated with the same doses per volume of IgG (clone TNP6A7, Bio X Cell) and control liposomes (or PBS as indicated, Liposoma). On day 0, mice were implanted orthotopically with 500,000 KPL86 cells and then treated with Bleo (1 mg/kg) on day 2.

PDGFRα cell depletion studies

To deplete PDGFRα^{+} cells, 8- to 12-week-old PDFGR^{DTR} mice and wild-type littermates were administered 2.0 mg of tamoxifen (Sigma-Aldrich) in 100 μl of PBS of corn oil per mouse for 5 days. On day 3 of tamoxifen injections, KPL86 cells were retro-orbitally injected as above at 500,000 cells per 100 μl of PBS (Trevigen). On day 5, mice received the fifth dose of tamoxifen in the early morning. Mice then received single-dose administration of either Bleo (1 mg/kg in 50 μl) or PBS (50 μl) and were intratracheally administered as described above. In the evening on day 5, they received 100 μl of diphtheria toxin (at 25 ng/g of body weight; catalog number: BML-G135-0001, Enzo Life Sciences) intraperitoneally. On days 7 and 9, mice received tamoxifen, and on days 8 and 10, mice received diphtheria toxin, as described above. Mice were euthanized on day 14.

Pulmonary TGFβ overexpression studies

Overexpression of TGFβ in the lung was achieved by administering AAV6-CMV-m-TGFB1 [AAV-274099; RefSeq no. for gene of interest (GOI) is BC013738; 3.3×10^{12} genome copies (GCs) per ml]. AAV6-CMV-Null (Vector Biosystems) was administered as a control. Three days after retro-orbital injection of KPL86 cells as above, 2.2×10^{10} GCs of AAV6-CMV-m-TGFB1 or AAV6-CMV-Null were administered intratracheally.

Tissue harvest

Mice were euthanized by intracardiac perfusion with 15 ml of PBS-heparin under isoflurane anesthesia. For flow cytometry experiments, CD45-eFluor605 was injected 5 min before euthanasia to exclude blood-derived CD45^{+} cells. Normal and tumor-bearing tissues were manually minced and digested in 20 ml of Hank's balanced salt solution (Thermo Fisher Scientific) supplemented with collagenase A (2 mg/ml; Roche) and 1× deoxyribonuclease I (DNase I; Sigma-Aldrich) for 30 min (20 min for normal tissue) at 37°C with agitation. After digestion, the cell suspensions were quenched with 5 ml of fetal bovine serum (FBS) and filtered through 40-μm nylon mesh. The filtered suspensions were then pelleted by centrifugation (1800 rpm for 4 min at 4°C) and resuspended in flow cytometry buffer [PBS containing 1% bovine serum albumin (BSA) and 5 mM EDTA] as a single-cell suspension.

Flow cytometry

After tissue digestion, single-cell suspensions were blocked with rat anti-mouse CD16/CD32 antibodies (eBioscience) for 10 min on ice and pelleted by centrifugation. The cells were subsequently labeled with 100 μl of fluorophore-conjugated anti-mouse extracellular antibodies at recommended dilutions for 30 min on ice in flow cytometry buffer. All antibodies are listed in data file S6. All samples were analyzed on X-20 cytometers.

Mass cytometry

Mouse tumor-bearing lung samples (six mice per group) were collected and digested in Hank's balanced salt solution supplemented with collagenase A (2 mg/ml; Roche) and DNase I at 37°C for 30 min with agitation to generate single-cell suspensions. Cell suspensions were counted, and 2 million cells per sample were taken for subsequent staining. Cells were stained in 5 μM cisplatin for 1 min on ice and washed with CyFACS buffer (PBS, 0.1% BSA, 0.02% NaN_3, and 2 mM EDTA) twice. The cells were then incubated with FcR blocking reagent (1:200 in CyFACS) for 10 min on ice, followed by surface-antibody cocktail for 40 min on ice. After incubation, surface marker–stained cells were washed twice with CyFACS buffer. Cells were then fixed with formaldehyde for 25 min on ice, after which permeabilization buffer was added for 5 min (00-5523-00, eBioscience). The cells were then washed once with permeabilization buffer and resuspended in permeabilization buffer containing the intracellular stain cocktail for 40 min on ice. All antibodies are listed in data file S7. The cells were then washed

and fixed a second time in 4% paraformaldehyde (PFA) in PBS at 4°C at least overnight. One day before acquisition, each sample was barcoded with a unique combination of palladium metal barcodes using the manufacturer's instructions (Fluidigm). After bar coding, the cells were pooled together and incubated overnight at 4°C in 2% PFA containing 40 nM iridium nucleic acid intercalator (Fluidigm). On the day of acquisition, the barcoded samples were washed and suspended in water containing 10% EQ Calibration Beads (Fluidigm) before acquisition on a CyTOF2 mass cytometer (Fluidigm).

Cells were normalized with the MATLAB normalizer (v.7.14.0.739 run in MATLAB R2012a). The normalized data were uploaded into Cytobank. Sample barcodes were interpreted using a single-cell debarcoder tool. Flow cytometry standard (FCS) files were then uploaded to Cytobank and manually gated to exclude normalization beads, cell debris, dead cells, doublets, and $CD45^-$ cells. The filtered sample from each individual specimen was then exported and analyzed using the R CATALYST package in R, version 3.8.2 (the R Project for Statistical Computing, Vienna, Austria). Briefly, FCS files were downsampled to equivalent cell counts before clustering with the R implementation of the Phenograph algorithm. All markers were used for clustering analysis, except for CD45 (already gated on in Cytobank), Ki67 (to avoid driving clustering on the basis of proliferation and not cell type), Ox40L, and CCR7 [low non-redundancy score (NRS)]. Dimensional reduction and visualization were performed using the UMAP algorithm. Last, differential cluster abundance testing and differential cluster expression testing were performed with the R diffcyt package using a generalized linear mixed model.

Single-cell RNA sequencing

Lung tissues were taken from three 12-week-old KPL GEMM mice treated with either PBS ($n = 3$) or Bleo ($n = 3$) and processed to single-cell suspension as explained in the tissue harvest section, and mice from each treatment group were pooled together and sorted for immune cells ($CD45^+$) or mesenchymal cells ($CD45^-$ $CD31^-$ $EpCAM^-$) using an Aria II cell sorter (BD Biosciences). Sorted cells from each sample were submitted to McDonnell Genome Institute at Washington University in St. Louis School of Medicine, where they were encapsulated into droplets, and libraries were prepared using Chromium Single Cell 3′ v3 Reagent kits according to the manufacturer's protocol (10x Genomics). The generated libraries were sequenced by a NovaSeq 6000 sequencing system (Illumina) to an average of 50,000 mean reads per cell. The Cellranger mkfastq pipeline (10x Genomics) was used to demultiplex illumine base call files to FASTQ files. Files from the PBS- or Bleo-treated tumor–bearing lungs were demultiplexed with >97% valid barcodes and >94% q30 reads. Afterward, FASTQ files from each sample were processed with Cellranger counts and aligned to the mm10 reference (v.3.1.0, 10x Genomics).

Mouse scRNA-seq data analysis

The filtered feature barcode matrix from the KPL lungs from PBS- or Bleo-treated mice were loaded into Seurat as Seurat objects (Seurat v.3). For each Seurat object, genes that were expressed in fewer than three cells and cells that expressed fewer than 1000 or more than 8000 genes were excluded. Cells with greater than 10% mitochondrial RNA content were also excluded. For immune cells, this resulted in 4491 and 7457 cells for PBS and Bleo, respectively. For CAFs, this resulted in 5812 and 13,575 cells for PBS and Bleo, respectively, which represents 87% of the total number of cells that were sorted, and the resulting single-cell RNA was filtered for purity, as described above. SCTransform with default parameters was used on each individual sample to normalize and scale the expression matrix against the sequence depths and percentages of mitochondrial genes. Principal components analysis (PCA) was performed on the 3000 variable genes calculated earlier (function RunPCA). A UMAP dimensional reduction was performed on the scaled matrix using the first 25 PCA components to obtain a two-dimensional representation of cell states. Then, these defined 25 dimensionalities were used to refine the edge weights between any two cells on the basis of Jaccard similarity (FindNeighbors) and were used to cluster cells through FindClusters functions, which implemented shared nearest-neighbor modularity optimization with a resolution of 0.3, leading to 21 clusters.

To characterize clusters, the FindAllMarkers function with log-fold threshold = 0.25 and minimum 0.25-fold difference and Model-based Analysis of Single-Cell Transcriptomics (MAST) test were used to identify signatures alone with each cluster. The macrophage/monocytes were selected, and the top 3000 variable features were recalculated to recluster to a higher resolution of 0.3. Macrophages were selected on the basis of clusters with high expressions of known macrophage marker genes, including *Csf1r*, *C1qa*, *C1qb*, and *H2-Aa*, confirmed by the absence of *Cd3e*, *Ms4a1*, *Krt19*, *Zbtb46*, and *Flt3*, and further confirmed by identifying DEGs associated with potential macrophage clusters when compared with known macrophage-specific marker genes. The fibroblasts were selected, and the top 3000 variable features were recalculated to recluster to a higher resolution of 0.3. Fibroblast subsets were defined by expression of *Col1a1*, *Tagln*, *Pdgfrb*, *Col14a1*, *Clec3b*, *Ly5c1*, *Col13a1*, *S100a1*, *Fn1*, *Saa3*, and *Acta2*.

Analysis of RNA-seq data

Gene expression data from the POPLAR (NCT01903993) and OAK (NCT02008227) clinical trial cohorts were accessed via EGAD00001008391 and EGAD00001008390. Clinical data were accessed via EGAD00001008549 and EGAD00001008548. Data were formatted in $\log_2$ transcript per million reads. Indicated gene signatures were calculated using the UCell gene set enrichment approach (*83*) in the escape R package (v1.4.1) (*84*). Absolute cell abundance deconvolution using the bulk sequencing was performed using CIBERSORT (*85*) using the based support vector machine model for cell types. Survival analysis was performed using the survival (v3.5-3) and survminer (v0.4.9) R packages. High/low survival cohorts were separated on the basis of optimal log-rank testing with the maximal ratio for calculation set at 85:15. Cox proportional hazard analysis was performed for binary comparisons. Pearson correlation was used to evaluate the relationship between a patients' Col13 CAF top 50 gene signature (data file S5) score with the described immune subset abundance from CIBERSORT after extracting the samples that had no available data for that cell type of interest. These data were imported to GraphPad Prism (version 9.3) for presentation purposes.

IHC staining

Mouse tissues were fixed in 10% formalin for 24 hours and embedded in paraffin after graded ethanol dehydration. Embedded tissues were sectioned into 6-μm sections using a microtome. TMAs LUC1021 and LUC1505 were obtained from Pantomics. Where

applicable, formalin-fixed, paraffin-embedded (FFPE) sections were stained for H&E (Thermo Fisher Scientific) or Masson's Trichrome (Diagnostic Biosystems). Where applicable, FFPE 6-μm sections loaded into a BOND R_Xm (Leica Biosystems) and stained with antibodies listed in data file S8. On the basis of antibody host species, default manufacturer's protocols were used (IntenseR and Polymer Refine), containing antigen-retrieval with citrate buffer, goat serum, and peroxide block; primary antibody incubation; and postprimary incubation, and chromogenically visualized with a 3,3′-diaminobenzidine (DAB) substrate. Images were obtained using a Axioscan Slide Scanner (Zeiss) and analyzed with HALO software (Indica Labs) with the default manufacturer's settings.

Coculture of BMDMs and primary lung fibroblasts

BMDMs were isolated as described previously (*86*). Briefly, bone marrow cells were isolated by flushing femurs and tibias from C57BL/6J mice and cultured in Dulbecco's modified Eagle's medium (DMEM)/F12 medium (Lonza) containing 10% FBS, penicillin-streptomycin (Gibco), and macrophage colony-stimulating factor (M-CSF; 20 ng/ml; PeproTech). Primary fibroblasts were isolated from mouse lungs treated with PBS or Bleo. Briefly, after right heart perfusion using sterile technique, lungs were manually minced and digested using 20 ml of Hank's balanced salt solution (Thermo Fisher Scientific) supplemented with collagenase A (2 mg/ml; Roche) and 1× DNase I (Sigma-Aldrich), which had been filtered through a 0.22-μm filter and then had G418/Gentamicin (50 μg/ml; Gibco) and amphotericin B (2.5 μg/ml; Gibco) added. The tissue was digested in the above solution for 25 min at 37°C with agitation. Digested tissue was filtered through a 100-μm filter into sterile DMEM/F12 medium (Lonza) containing 10% FBS, penicillin-streptomycin (Gibco), as well as G418/Gentamicin (50 μg/ml; Gibco) and amphotericin B (2.5 μg/ml, Gibco). After 5 days in culture, adherent macrophages or primary fibroblasts were harvested. BMDMs were seeded on six-well plate, and fibroblasts from PBS- or Bleo-treated lungs were cultured on Transwell membranes (353090, Corning) in six-well plates. The following day, fibroblasts on transwell membranes were placed into the six-well plates with BMDMs in DMEM/F12 medium (Lonza) containing 10% FBS, penicillin-streptomycin (Gibco), and M-CSF (20 ng/ml; PeproTech). BMDMs were harvested 24 hours later. The medium was removed, and cells were rinsed with PBS before RNA isolation.

RNA isolation and real-time polymerase chain reaction

Total RNA was extracted from cells using an E.Z.N.A. Total RNA Kit (Omega). cDNAs were synthesized using qScript cDNA SuperMix (QuantaBio). Quantitative real-time polymerase chain reaction (PCR) TaqMan primer probe sets (Applied Biosystems) were used. Relative gene expression was determined on an ABI 7900HT quantitative PCR machine (ABI Biosystems) using TaqMan Gene Expression Master Mix (Applied Biosystems). Glyceraldehyde-3-phosphate dehydrogenase (*GAPDH*), TATA box–binding protein (*TBP*), and hypoxanthine phosphoribosyl transferase (*HPRT*) were used for normalization of gene expression to calculate the fold changes in gene expression.

Statistics

All raw, individual-level data for experiments where $n < 20$ are presented in data file S9. Statistical analyses were performed by GraphPad Prism (version 9.3). For comparison of multiple groups, a one-way analysis of variance with a multiple-comparison test was used. A chi-square test was used for continuous variables. For comparison of two groups (except in scRNA-seq data), the two-sided, unpaired *t* test was used. *P* values of less than 0.05 were considered statistically significant and are labeled with single asterisks. For GSEA comparisons, the $\log_2$ (fold change) of all genes detected with min.pct > 0.1 and past MAST test was used as a ranking metric. GSEA was performed using Gene Ontology terms, Kyoto Encyclopedia of Genes and Genomes pathways, Reactome, and MsigDB gene sets with a Benjamini-Hochberg false discovery rate of <0.05 in ClusterProfiler. For DEGs between the two groups in each mouse NSCLC model, we filtered genes with a Bonferroni-corrected $P < 0.05$ and a fold change of >1.2 or <0.8.

Supplementary Materials

This PDF file includes:
Fig. S1 to S6

Other Supplementary Material for this manuscript includes the following:
Data files S1 to S9
MDAR Reproducibility Checklist

View/request a protocol for this paper from *Bio-protocol*.

REFERENCES AND NOTES

1. R. L. Siegel, K. D. Miller, H. E. Fuchs, A. Jemal, Cancer Statistics, 2021. *CA Cancer J. Clin.* **71**, 7–33 (2021).
2. L. A. Torre, R. L. Siegel, A. Jemal, in *Lung Cancer and Personalized Medicine: Current Knowledge and Therapies*, A. Ahmad, S. Gadgeel, Eds. (Springer International Publishing, 2016), pp. 1–19.
3. L. Paz-Ares, A. Luft, D. Vicente, A. Tafreshi, M. Gumus, J. Mazieres, B. Hermes, F. Cay Senler, T. Csoszi, A. Fulop, J. Rodriguez-Cid, J. Wilson, S. Sugawara, T. Kato, K. H. Lee, Y. Cheng, S. Novello, B. Halmos, X. Li, G. M. Lubiniecki, B. Piperdi, D. M. Kowalski; KEYNOTE-407 Investigators, Pembrolizumab plus chemotherapy for squamous non-small-cell lung cancer. *N. Engl. J. Med.* **379**, 2040–2051 (2018).
4. M. Reck, D. Rodriguez-Abreu, A. G. Robinson, R. Hui, T. Csőszi, A. Fülöp, M. Gottfried, N. Peled, A. Tafreshi, S. Cuffe, M. O'Brien, S. Rao, K. Hotta, M. A. Leiby, G. M. Lubiniecki, Y. Shentu, R. Rangwala, J. R. Brahmer; KEYNOTE-024 Investigators, Pembrolizumab versus chemotherapy for PD-L1-positive non-small-cell lung cancer. *N. Engl. J. Med.* **375**, 1823–1833 (2016).
5. L. Gandhi, D. Rodríguez-Abreu, S. Gadgeel, E. Esteban, E. Felip, F. De Angelis, M. Domine, P. Clingan, M. J. Hochmair, S. F. Powell, S. Y. Cheng, H. G. Bischoff, N. Peled, F. Grossi, R. R. Jennens, M. Reck, R. Hui, E. B. Garon, M. Boyer, B. Rubio-Viqueira, S. Novello, T. Kurata, J. E. Gray, J. Vida, Z. Wei, J. Yang, H. Raftopoulos, M. C. Pietanza, M. C. Garassino; KEYNOTE-189 Investigators, Pembrolizumab plus chemotherapy in metastatic non-small-cell lung cancer. *N. Engl. J. Med.* **378**, 2078–2092 (2018).
6. M. D. Hellmann, L. Paz-Ares, R. Bernabe Caro, B. Zurawski, S. W. Kim, E. Carcereny Costa, K. Park, A. Alexandru, L. Lupinacci, E. de la Mora Jimenez, H. Sakai, I. Albert, A. Vergnenegre, S. Peters, K. Syrigos, F. Barlesi, M. Reck, H. Borghaei, J. R. Brahmer, K. J. O'Byrne, W. J. Geese, P. Bhagavatheeswaran, S. K. Rabindran, R. S. Kasinathan, F. E. Nathan, S. S. Ramalingam, Nivolumab plus Ipilimumab in advanced non-small-cell lung cancer. *N. Engl. J. Med.* **381**, 2020–2031 (2019).
7. J. A. Burger, A. Tedeschi, P. M. Barr, T. Robak, C. Owen, P. Ghia, O. Bairey, P. Hillmen, N. L. Bartlett, J. Li, D. Simpson, S. Grosicki, S. Devereux, H. McCarthy, S. Coutre, H. Quach, G. Gaidano, Z. Maslyak, D. A. Stevens, A. Janssens, F. Offner, J. Mayer, M. O'Dwyer, A. Hellmann, A. Schuh, T. Siddiqi, A. Polliack, C. S. Tam, D. Suri, M. Cheng, F. Clow, L. Styles, D. F. James, T. J. Kipps; RESONATE-2 Investigators, Ibrutinib as initial therapy for patients with chronic lymphocytic leukemia. *N. Engl. J. Med.* **373**, 2425–2437 (2015).
8. F. Skoulidis, M. E. Goldberg, D. M. Greenawalt, M. D. Hellmann, M. M. Awad, J. F. Gainor, A. B. Schrock, R. J. Hartmaier, S. E. Trabucco, L. Gay, S. M. Ali, J. A. Elvin, G. Singal, J. S. Ross, D. Fabrizio, P. M. Szabo, H. Chang, A. Sasson, S. Srinivasan, S. Kirov, J. Szustakowski, P. Vitazka, R. Edwards, J. A. Bufill, N. Sharma, S.-H. I. Ou, N. Peled, D. R. Spigel, H. Rizvi, E. J. Aguilar, B. W. Carter, J. Erasmus, D. F. Halpenny, A. J. Plodkowski, N. M. Long, M. Nishino,

W. L. Denning, A. Galan-Cobo, H. Hamdi, T. Hirz, P. Tong, J. Wang, J. Rodriguez-Canales, P. A. Villalobos, E. R. Parra, N. Kalhor, L. M. Sholl, J. L. Sauter, A. A. Jungbluth, M. Mino-Kenudson, R. Azimi, Y. Y. Elamin, J. Zhang, G. C. Leonardi, F. Jiang, K.-K. Wong, J. J. Lee, V. A. Papadimitrakopoulou, I. I. Wistuba, V. A. Miller, G. M. Frampton, J. D. Wolchok, A. T. Shaw, P. A. Jänne, P. J. Stephens, C. M. Rudin, W. J. Geese, L. A. Albacker, J. V. Heymach, *STK11/LKB1* mutations and PD-1 inhibitor resistance in *KRAS*-mutant lung adenocarcinoma. *Cancer Discov.* **8**, 822–835 (2018).

9. H. Hu, Z. Piotrowska, P. J. Hare, H. Chen, H. E. Mulvey, A. Mayfield, S. Noeen, K. Kattermann, M. Greenberg, A. Williams, A. K. Riley, J. J. Wilson, Y.-Q. Mao, R.-P. Huang, M. K. Banwait, J. Ho, G. S. Crowther, L. P. Hariri, R. S. Heist, D. P. Kodack, L. Pinello, A. T. Shaw, M. Mino-Kenudson, A. N. Hata, L. V. Sequist, C. H. Benes, M. J. Niederst, J. A. Engelman, Three subtypes of lung cancer fibroblasts define distinct therapeutic paradigms. *Cancer Cell* **39**, 1531–1547.e10 (2021).
10. M. Binnewies, E. W. Roberts, K. Kersten, V. Chan, D. F. Fearon, M. Merad, L. M. Coussens, D. I. Gabrilovich, S. Ostrand-Rosenberg, C. C. Hedrick, R. H. Vonderheide, M. J. Pittet, R. K. Jain, W. Zou, T. K. Howcroft, E. C. Woodhouse, R. A. Weinberg, M. F. Krummel, Understanding the tumor immune microenvironment (TIME) for effective therapy. *Nat. Med.* **24**, 541–550 (2018).
11. J. Goc, C. Germain, T. K. Vo-Bourgais, A. Lupo, C. Klein, S. Knockaert, L. de Chaisemartin, H. Ouakrim, E. Becht, M. Alifano, P. Validire, R. Remark, S. A. Hammond, I. Cremer, D. Damotte, W.-H. Fridman, C. Sautès-Fridman, M.-C. Dieu-Nosjean, Dendritic cells in tumor-associated tertiary lymphoid structures signal a Th1 cytotoxic immune contexture and license the positive prognostic value of infiltrating $CD8^+$ T cells. *Cancer Res.* **74**, 705–715 (2014).
12. Y. Geng, Y. Shao, W. He, W. Hu, Y. Xu, J. Chen, C. Wu, J. Jiang, Prognostic role of tumor-infiltrating lymphocytes in lung cancer: A meta-analysis. *Cell. Physiol. Biochem.* **37**, 1560–1571 (2015).
13. S. M. O'Brien, A. Klampatsa, J. C. Thompson, M. C. Martinez, W.-T. Hwang, A. S. Rao, J. E. Standalick, S. Kim, E. Cantu, L. A. Litzky, S. Singhal, E. B. Eruslanov, E. K. Moon, S. M. Albelda, Function of human tumor-infiltrating lymphocytes in early-stage non-small cell lung cancer. *Cancer Immunol. Res.* **7**, 896–909 (2019).
14. S. Spranger, Mechanisms of tumor escape in the context of the T-cell-inflamed and the non-T-cell-inflamed tumor microenvironment. *Int. Immunol.* **28**, 383–391 (2016).
15. K. Hildner, B. T. Edelson, W. E. Purtha, M. Diamond, H. Matsushita, M. Kohyama, B. Calderon, B. U. Schraml, E. R. Unanue, M. S. Diamond, R. D. Schreiber, T. L. Murphy, K. M. Murphy, *Batf3* deficiency reveals a critical role for $CD8\alpha^+$ dendritic cells in cytotoxic T cell immunity. *Science* **322**, 1097–1100 (2008).
16. M. B. Fuertes, A. K. Kacha, J. Kline, S.-R. Woo, D. M. Kranz, K. M. Murphy, T. F. Gajewski, Host type I IFN signals are required for antitumor $CD8^+$ T cell responses through $CD8\alpha^+$ dendritic cells. *J. Exp. Med.* **208**, 2005–2016 (2011).
17. J. J. Engelhardt, B. Boldajipour, P. Beemiller, P. Pandurangi, C. Sorensen, Z. Werb, M. Egeblad, M. F. Krummel, Marginating dendritic cells of the tumor microenvironment cross-present tumor antigens and stably engage tumor-specific T cells. *Cancer Cell* **21**, 402–417 (2012).
18. M. L. Broz, M. Binnewies, B. Boldajipour, A. E. Nelson, J. L. Pollack, D. J. Erle, A. Barczak, M. D. Rosenblum, A. Daud, D. L. Barber, S. Amigorena, L. J. Van't Veer, A. I. Sperling, D. M. Wolf, M. F. Krummel, Dissecting the tumor myeloid compartment reveals rare activating antigen-presenting cells critical for T cell immunity. *Cancer Cell* **26**, 638–652 (2014).
19. I. G. House, P. Savas, J. Lai, A. X. Y. Chen, A. J. Oliver, Z. L. Teo, K. L. Todd, M. A. Henderson, L. Giuffrida, E. V. Petley, K. Sek, S. Mardiana, T. N. Gide, C. Quek, R. A. Scolyer, G. V. Long, J. S. Wilmott, S. Loi, P. K. Darcy, P. A. Beavis, Macrophage-derived CXCL9 and CXCL10 are required for antitumor immune responses following immune checkpoint blockade. *Clin. Cancer Res.* **26**, 487–504 (2020).
20. M. E. Mikucki, D. T. Fisher, J. Matsuzaki, J. J. Skitzki, N. B. Gaulin, J. B. Muhitch, A. W. Ku, J. G. Frelinger, K. Odunsi, T. F. Gajewski, A. D. Luster, S. S. Evans, Non-redundant requirement for CXCR3 signalling during tumoricidal T-cell trafficking across tumour vascular checkpoints. *Nat. Commun.* **6**, 7458 (2015).
21. A. Schnell, L. Bod, A. Madi, V. K. Kuchroo, The yin and yang of co-inhibitory receptors: Toward anti-tumor immunity without autoimmunity. *Cell Res.* **30**, 285–299 (2020).
22. S. A. Fuertes Marraco, N. J. Neubert, G. Verdeil, D. E. Speiser, Inhibitory receptors beyond T cell exhaustion. *Front. Immunol.* **6**, 310 (2015).
23. K. Wing, Y. Onishi, P. Prieto-Martin, T. Yamaguchi, M. Miyara, Z. Fehervari, T. Nomura, S. Sakaguchi, CTLA-4 control over $Foxp3^+$ regulatory T cell function. *Science* **322**, 271–275 (2008).
24. A.-P. Ganesan, M. Johansson, B. Ruffell, A. Yagui-Beltrán, A. Beltran, J. Lau, D. M. Jablons, L. M. Coussens, Tumor-infiltrating regulatory T cells inhibit endogenous cytotoxic T cell responses to lung adenocarcinoma. *J. Immunol.* **191**, 2009–2017 (2013).
25. R. Z. Panni, J. M. Herndon, C. Zuo, S. Hegde, G. D. Hogg, B. L. Knolhoff, M. A. Breden, X. Li, V. E. Krisnawan, S. Q. Khan, J. K. Schwarz, B. E. Rogers, R. C. Fields, W. G. Hawkins, V. Gupta, D. G. DeNardo, Agonism of CD11b reprograms innate immunity to sensitize pancreatic cancer to immunotherapies. *Sci. Transl. Med.* **11**, eaau9240 (2019).
26. D. G. DeNardo, B. Ruffell, Macrophages as regulators of tumour immunity and immunotherapy. *Nat. Rev. Immunol.* **19**, 369–382 (2019).
27. M. Casanova-Acebes, E. Dalla, A. M. Leader, J. LeBerichel, J. Nikolic, B. M. Morales, M. Brown, C. Chang, L. Troncoso, S. T. Chen, A. Sastre-Perona, M. D. Park, A. Tabachnikova, M. Dhainaut, P. Hamon, B. Maier, C. M. Sawai, E. Agulló-Pascual, M. Schober, B. D. Brown, B. Reizis, T. Marron, E. Kenigsberg, C. Moussion, P. Benaroch, J. A. Aguirre-Ghiso, M. Merad, Tissue-resident macrophages provide a pro-tumorigenic niche to early NSCLC cells. *Nature* **595**, 578–584 (2021).
28. H. Jiang, S. Hegde, B. L. Knolhoff, Y. Zhu, J. M. Herndon, M. A. Meyer, T. M. Nywening, W. G. Hawkins, I. M. Shapiro, D. T. Weaver, J. A. Pachter, A. Wang-Gillam, D. G. DeNardo, Targeting focal adhesion kinase renders pancreatic cancers responsive to checkpoint immunotherapy. *Nat. Med.* **22**, 851–860 (2016).
29. S. Hegde, V. E. Krisnawan, B. H. Herzog, C. Zuo, M. A. Breden, B. L. Knolhoff, G. D. Hogg, J. P. Tang, J. M. Baer, C. Mpoy, K. B. Lee, K. A. Alexander, B. E. Rogers, K. M. Murphy, W. G. Hawkins, R. C. Fields, C. J. DeSelm, J. K. Schwarz, D. G. DeNardo, Dendritic cell paucity leads to dysfunctional immune surveillance in pancreatic cancer. *Cancer Cell* **37**, 289–307.e9 (2020).
30. E. Sahai, I. Astsaturov, E. Cukierman, D. G. DeNardo, M. Egeblad, R. M. Evans, D. Fearon, F. R. Greten, S. R. Hingorani, T. Hunter, R. O. Hynes, R. K. Jain, T. Janowitz, C. Jorgensen, A. C. Kimmelman, M. G. Kolonin, R. G. Maki, R. S. Powers, E. Pure, D. C. Ramirez, R. Scherz-Shouval, M. H. Sherman, S. Stewart, T. D. Tlsty, D. A. Tuveson, F. M. Watt, V. Weaver, A. T. Weeraratna, Z. Werb, A framework for advancing our understanding of cancer-associated fibroblasts. *Nat. Rev. Cancer* **20**, 174–186 (2020).
31. C. Hutton, F. Heider, A. Blanco-Gomez, A. Banyard, A. Kononov, X. Zhang, S. Karim, V. Paulus-Hock, D. Watt, N. Steele, S. Kemp, E. K. J. Hogg, J. Kelly, R. F. Jackstadt, F. Lopes, M. Menotti, L. Chisholm, A. Lamarca, J. Valle, O. J. Sansom, C. Springer, A. Malliri, R. Marais, M. Pasca di Magliano, S. Zelenay, J. P. Morton, C. Jørgensen, Single-cell analysis defines a pancreatic fibroblast lineage that supports anti-tumor immunity. *Cancer Cell* **39**, 1227–1244.e20 (2021).
32. P. P. Provenzano, C. Cuevas, A. E. Chang, V. K. Goel, D. D. Von Hoff, S. R. Hingorani, Enzymatic targeting of the stroma ablates physical barriers to treatment of pancreatic ductal adenocarcinoma. *Cancer Cell* **21**, 418–429 (2012).
33. B. C. Özdemir, T. Pentcheva-Hoang, J. L. Carstens, X. Zheng, C.-C. Wu, T. R. Simpson, H. Laklai, H. Sugimoto, C. Kahlert, S. V. Novitskiy, A. De Jesus-Acosta, P. Sharma, P. Heidari, U. Mahmood, L. Chin, H. L. Moses, V. M. Weaver, A. Maitra, J. P. Allison, V. S. LeBleu, R. Kalluri, Depletion of carcinoma-associated fibroblasts and fibrosis induces immunosuppression and accelerates pancreas cancer with reduced survival. *Cancer Cell* **25**, 719–734 (2014).
34. M. W. Conklin, J. C. Eickhoff, K. M. Riching, C. A. Pehlke, K. W. Eliceiri, P. P. Provenzano, A. Friedl, P. J. Keely, Aligned collagen is a prognostic signature for survival in human breast carcinoma. *Am. J. Pathol.* **178**, 1221–1232 (2011).
35. E. Brauchle, J. Kasper, R. Daum, N. Schierbaum, C. Falch, A. Kirschniak, T. E. Schaffer, K. Schenke-Layland, Biomechanical and biomolecular characterization of extracellular matrix structures in human colon carcinomas. *Matrix Biol.* **68-69**, 180–193 (2018).
36. Y. Takahashi, G. Ishii, T. Taira, S. Fujii, S. Yanagi, T. Hishida, J. Yoshida, M. Nishimura, H. Nomori, K. Nagai, A. Ochiai, Fibrous stroma is associated with poorer prognosis in lung squamous cell carcinoma patients. *J. Thorac. Oncol.* **6**, 1460–1467 (2011).
37. K. Suzuki, T. Yokose, J. Yoshida, M. Nishimura, K. Takahashi, K. Nagai, Y. Nishiwaki, Prognostic significance of the size of central fibrosis in peripheral adenocarcinoma of the lung. *Ann. Thorac. Surg.* **69**, 893–897 (2000).
38. A. M. Maeshima, T. Niki, A. Maeshima, T. Yamada, H. Kondo, Y. Matsuno, Modified scar grade: A prognostic indicator in small peripheral lung adenocarcinoma. *Cancer* **95**, 2546–2554 (2002).
39. M. R. Wick, Pathologic features of smoking-related lung diseases, with emphasis on smoking-related interstitial fibrosis and a consideration of differential diagnoses. *Semin. Diagn. Pathol.* **35**, 315–323 (2018).
40. B. Ballester, J. Milara, J. Cortijo, Idiopathic pulmonary fibrosis and lung cancer: Mechanisms and molecular targets. *Int. J. Mol. Sci.* **20**, 593 (2019).
41. N. Kim, H. K. Kim, K. Lee, Y. Hong, J. H. Cho, J. W. Choi, J.-I. Lee, Y.-L. Suh, B. M. Ku, H. H. Eum, S. Choi, Y.-L. Choi, J.-G. Joung, W.-Y. Park, H. A. Jung, J.-M. Sun, S.-H. Lee, J. S. Ahn, K. Park, M.-J. Ahn, H.-O. Lee, Single-cell RNA sequencing demonstrates the molecular and cellular reprogramming of metastatic lung adenocarcinoma. *Nat. Commun.* **11**, 2285 (2020).
42. D. Lambrechts, E. Wauters, B. Boeckx, S. Aibar, D. Nittner, O. Burton, A. Bassez, H. Decaluwé, A. Pircher, K. Van den Eynde, B. Weynand, E. Verbeken, P. De Leyn, A. Liston, J. Vansteenkiste, P. Carmeliet, S. Aerts, B. Thienpont, Phenotype molding of stromal cells in the lung tumor microenvironment. *Nat. Med.* **24**, 1277–1289 (2018).
43. D. H. Peng, B. L. Rodriguez, L. Diao, L. Chen, J. Wang, L. A. Byers, Y. Wei, H. A. Chapman, M. Yamauchi, C. Behrens, G. Raso, L. M. S. Soto, E. R. P. Cuentes, I. I. Wistuba, J. M. Kurie,

D. L. Gibbons, Collagen promotes anti-PD-1/PD-L1 resistance in cancer through LAIR1-dependent CD8$^+$ T cell exhaustion. *Nat. Commun.* **11**, 4520 (2020).
44. M. DuPage, A. L. Dooley, T. Jacks, Conditional mouse lung cancer models using adenoviral or lentiviral delivery of Cre recombinase. *Nat. Protoc.* **4**, 1064–1072 (2009).
45. B. B. Moore, C. M. Hogaboam, Murine models of pulmonary fibrosis. *Am. J. Physiol. Lung Cell. Mol. Physiol.* **294**, L152–L160 (2008).
46. T. Schneider, H. Hoffmann, H. Dienemann, P. A. Schnabel, A. H. Enk, S. Ring, K. Mahnke, Non-small cell lung cancer induces an immunosuppressive phenotype of dendritic cells in tumor microenvironment by upregulating B7-H3. *J. Thorac. Oncol.* **6**, 1162–1168 (2011).
47. L. Ombrato, E. Nolan, I. Kurelac, A. Mavousian, V. L. Bridgeman, I. Heinze, P. Chakravarty, S. Horswell, E. Gonzalez-Gualda, G. Matacchione, A. Weston, J. Kirkpatrick, E. Husain, V. Speirs, L. Collinson, A. Ori, J.-H. Lee, I. Malanchi, Metastatic-niche labelling reveals parenchymal cells with stem features. *Nature* **572**, 603–608 (2019).
48. N. Caronni, G. M. Piperno, F. Simoncello, O. Romano, S. Vodret, Y. Yanagihashi, R. Dress, C.-A. Dutertre, M. Bugatti, P. Bourdeley, A. Del Prete, T. Schioppa, E. M. C. Mazza, L. Collavin, S. Zacchigna, R. Ostuni, P. Guermonprez, W. Vermi, F. Ginhoux, S. Bicciato, S. Nagata, F. Benvenuti, TIM4 expression by dendritic cells mediates uptake of tumor-associated antigens and anti-tumor responses. *Nat. Commun.* **12**, 2237 (2021).
49. M. J. Schliekelman, C. J. Creighton, B. N. Baird, Y. Chen, P. Banerjee, N. Bota-Rabassedas, Y.-H. Ahn, J. D. Roybal, F. Chen, Y. Zhang, D. K. Mishra, M. P. Kim, X. Liu, B. Mino, P. Villalobos, J. Rodriguez-Canales, C. Behrens, I. I. Wistuba, S. M. Hanash, J. M. Kurie, Thy-1$^+$ cancer-associated fibroblasts adversely impact lung cancer prognosis. *Sci. Rep.* **7**, 6478 (2017).
50. T. K. Kilvaer, M. R. Khanehkenari, T. Hellevik, S. Al-Saad, E.-E. Paulsen, R. M. Bremnes, L.-T. Busund, T. Donnem, I. Z. Martinez, Cancer associated fibroblasts in stage I-IIIA NSCLC: Prognostic impact and their correlations with tumor molecular markers. *PLOS ONE* **10**, e0134965 (2015).
51. T. Xie, Y. Wang, N. Deng, G. Huang, F. Taghavifar, Y. Geng, N. Liu, V. Kulur, C. Yao, P. Chen, Z. Liu, B. Stripp, J. Tang, J. Liang, P. W. Noble, D. Jiang, Single-cell deconvolution of fibroblast heterogeneity in mouse pulmonary fibrosis. *Cell Rep.* **22**, 3625–3640 (2018).
52. A. Mor, M. Segal Salto, A. Katav, N. Barashi, V. Edelshtein, M. Manetti, Y. Levi, J. George, M. Matucci-Cerinic, Blockade of CCL24 with a monoclonal antibody ameliorates experimental dermal and pulmonary fibrosis. *Ann. Rheum. Dis.* **78**, 1260–1268 (2019).
53. F. Li, X. Xu, J. Geng, X. Wan, H. Dai, The autocrine CXCR4/CXCL12 axis contributes to lung fibrosis through modulation of lung fibroblast activity. *Exp. Ther. Med.* **19**, 1844–1854 (2020).
54. N. Mukaida, S.-I. Sasaki, T. Baba, CCL4 signaling in the tumor microenvironment. *Adv. Exp. Med. Biol.* **1231**, 23–32 (2020).
55. B. Li, S. Zhang, N. Huang, H. Chen, P. Wang, J. Yang, Z. Li, CCL9/CCR1 induces myeloid-derived suppressor cell recruitment to the spleen in a murine H22 orthotopic hepatoma model. *Oncol. Rep.* **41**, 608–618 (2019).
56. R. Mezzapelle, M. Leo, F. Caprioglio, L. S. Colley, A. Lamarca, L. Sabatino, V. Colantuoni, M. P. Crippa, M. E. Bianchi, CXCR4/CXCL12 activities in the tumor microenvironment and implications for tumor immunotherapy. *Cancers (Basel)* **14**, 2314 (2022).
57. D. Zboralski, K. Hoehlig, D. Eulberg, A. Frömming, A. Vater, Increasing tumor-infiltrating T cells through inhibition of CXCL12 with NOX-A12 synergizes with PD-1 blockade. *Cancer Immunol. Res.* **5**, 950–956 (2017).
58. B. J. Marsland, P. Bättig, M. Bauer, C. Ruedl, U. Lässing, R. R. Beerli, K. Dietmeier, L. Ivanova, T. Pfister, L. Vogt, H. Nakano, C. Nembrini, P. Saudan, M. Kopf, M. F. Bachmann, CCL19 and CCL21 induce a potent proinflammatory differentiation program in licensed dendritic cells. *Immunity* **22**, 493–505 (2005).
59. S. Hillinger, S.-C. Yang, R. K. Batra, R. M. Strieter, W. Weder, S. M. Dubinett, S. Sharma, CCL19 reduces tumour burden in a model of advanced lung cancer. *Br. J. Cancer* **94**, 1029–1034 (2006).
60. K. Kohli, V. G. Pillarisetty, T. S. Kim, Key chemokines direct migration of immune cells in solid tumors. *Cancer Gene Ther.* **29**, 10–21 (2022).
61. N. Karin, Chemokines and cancer: New immune checkpoints for cancer therapy. *Curr. Opin. Immunol.* **51**, 140–145 (2018).
62. M.-I. Chung, M. Bujnis, C. E. Barkauskas, Y. Kobayashi, B. L. M. Hogan, Niche-mediated BMP/SMAD signaling regulates lung alveolar stem cell proliferation and differentiation. *Development* **145**, dev163014 (2018).
63. T. Buch, F. L. Heppner, C. Tertilt, T. J. Heinen, M. Kremer, F. T. Wunderlich, S. Jung, A. Waisman, A Cre-inducible diphtheria toxin receptor mediates cell lineage ablation after toxin administration. *Nat. Methods* **2**, 419–426 (2005).
64. I. E. Fernandez, O. Eickelberg, The impact of TGF-β on lung fibrosis: From targeting to biomarkers. *Proc. Am. Thorac. Soc.* **9**, 111–116 (2012).
65. A. Santana, B. Saxena, N. A. Noble, L. I. Gold, B. C. Marshall, Increased expression of transforming growth factor beta isoforms (beta 1, beta 2, beta 3) in bleomycin-induced pulmonary fibrosis. *Am. J. Respir. Cell Mol. Biol.* **13**, 34–44 (1995).
66. N. S. Patil, B. Y. Nabet, S. Müller, H. Koeppen, W. Zou, J. Giltnane, A. Au-Yeung, S. Srivats, J. H. Cheng, C. Takahashi, P. E. de Almeida, A. S. Chitre, J. L. Grogan, L. Rangell, S. Jayakar, M. Peterson, A. W. Hsia, W. E. O'Gorman, M. Ballinger, R. Banchereau, D. S. Shames, Intratumoral plasma cells predict outcomes to PD-L1 blockade in non-small cell lung cancer. *Cancer Cell* **40**, 289–300.e4 (2022).
67. H. F. Dvorak, Tumors: Wounds that do not heal-redux. *Cancer Immunol. Res.* **3**, 1–11 (2015).
68. S.-H. Kim, S.-I. Go, D. H. Song, S. W. Park, H. R. Kim, I. Jang, J. D. Kim, J. S. Lee, G.-W. Lee, Prognostic impact of CD8 and programmed death-ligand 1 expression in patients with resectable non-small cell lung cancer. *Br. J. Cancer* **120**, 547–554 (2019).
69. Y. Lan, M. Moustafa, M. Knoll, C. Xu, J. Furkel, A. Lazorchak, T.-L. Yeung, S.-M. Hasheminasab, M. H. Jenkins, S. Meister, H. Yu, J. Schlegel, B. Marelli, Z. Tang, G. Qin, C. Klein, J. Qi, C. Zhou, G. Locke, D. Krunic, M. G. Derner, C. Schwager, R. E. Fontana, K. Kriegsmann, F. Jiang, K. Rein, M. Kriegsmann, J. Debus, K.-M. Lo, A. Abdollahi, Simultaneous targeting of TGF-β/PD-L1 synergizes with radiotherapy by reprogramming the tumor microenvironment to overcome immune evasion. *Cancer Cell* **39**, 1388–1403.e10 (2021).
70. M. Cabeza-Cabrerizo, C. M. Minutti, M. P. da Costa, A. Cardoso, R. P. Jenkins, J. Kulikauskaite, M. D. Buck, C. Piot, N. Rogers, S. Crotta, L. Whittaker, H. H. Encabo, J. W. McCauley, J. E. Allen, M. Pasparakis, A. Wack, E. Sahai, E. S. C. Reis, Recruitment of dendritic cell progenitors to foci of influenza A virus infection sustains immunity. *Sci Immunol* **6**, eabi9331 (2021).
71. S. P. Arlauckas, S. B. Garren, C. S. Garris, R. H. Kohler, J. Oh, M. J. Pittet, R. Weissleder, Arg1 expression defines immunosuppressive subsets of tumor-associated macrophages. *Theranostics* **8**, 5842–5854 (2018).
72. O. R. Colegio, N.-Q. Chu, A. L. Szabo, T. Chu, A. M. Rhebergen, V. Jairam, N. Cyrus, C. E. Brokowski, S. C. Eisenbarth, G. M. Phillips, G. W. Cline, A. J. Phillips, R. Medzhitov, Functional polarization of tumour-associated macrophages by tumour-derived lactic acid. *Nature* **513**, 559–563 (2014).
73. T. Kwak, F. Wang, H. Deng, T. Condamine, V. Kumar, M. Perego, A. Kossenkov, L. J. Montaner, X. Xu, W. Xu, C. Zheng, L. M. Schuchter, R. K. Amaravadi, T. C. Mitchell, G. C. Karakousis, C. Mulligan, B. Nam, G. Masters, N. Hockstein, J. Bennett, Y. Nefedova, D. I. Gabrilovich, Distinct populations of immune-suppressive macrophages differentiate from monocytic myeloid-derived suppressor cells in cancer. *Cell Rep.* **33**, 108571 (2020).
74. S. J. Turley, V. Cremasco, J. L. Astarita, Immunological hallmarks of stromal cells in the tumour microenvironment. *Nat. Rev. Immunol.* **15**, 669–682 (2015).
75. A. T. Baker, M. H. Abuwarwar, L. Poly, S. Wilkins, A. L. Fletcher, Cancer-associated fibroblasts and T cells: From mechanisms to outcomes. *J. Immunol.* **206**, 310–320 (2021).
76. R. Barrett, E. Puré, Cancer-associated fibroblasts: Key determinants of tumor immunity and immunotherapy. *Curr. Opin. Immunol.* **64**, 80–87 (2020).
77. E. Batlle, J. Massagué, Transforming growth factor-β signaling in immunity and cancer. *Immunity* **50**, 924–940 (2019).
78. R. B. Holmgaard, D. A. Schaer, Y. Li, S. P. Castaneda, M. Y. Murphy, X. Xu, I. Inigo, J. Dobkin, J. R. Manro, P. W. Iversen, D. Surguladze, G. E. Hall, R. D. Novosiadly, K. A. Benhadji, G. D. Plowman, M. Kalos, K. E. Driscoll, Targeting the TGFβ pathway with galunisertib, a TGFβRI small molecule inhibitor, promotes anti-tumor immunity leading to durable, complete responses, as monotherapy and in combination with checkpoint blockade. *J. Immunother. Cancer* **6**, 47 (2018).
79. D. A. Schaer, S. Geeganage, N. Amaladas, Z. H. Lu, E. R. Rasmussen, A. Sonyi, D. Chin, A. Capen, Y. Li, C. M. Meyer, B. D. Jones, X. Huang, S. Luo, C. Carpenito, K. D. Roth, A. Nikolayev, B. Tan, M. Brahmachary, K. Chodavarapu, F. C. Dorsey, J. R. Manro, T. N. Doman, G. P. Donoho, D. Surguladze, G. E. Hall, M. Kalos, R. D. Novosiadly, The folate pathway inhibitor pemetrexed pleiotropically enhances effects of cancer immunotherapy. *Clin. Cancer Res.* **25**, 7175–7188 (2019).
80. C.-S. Lu, C.-W. Lin, Y.-H. Chang, H.-Y. Chen, W.-C. Chung, W.-Y. Lai, C.-C. Ho, T.-H. Wang, C.-Y. Chen, C.-L. Yeh, S. Wu, S.-P. Wang, P.-C. Yang, Antimetabolite pemetrexed primes a favorable tumor microenvironment for immune checkpoint blockade therapy. *J. Immunother. Cancer* **8**, e001392 (2020).
81. A. Vankerckhoven, T. Baert, M. Riva, C. De Bruyn, G. Thirion, K. Vandenbrande, J. Ceusters, I. Vergote, A. Coosemans, Type of chemotherapy has substantial effects on the immune system in ovarian cancer. *Transl. Oncol.* **14**, 101076 (2021).
82. N. T. H. Truong, T. Gargett, M. P. Brown, L. M. Ebert, Effects of chemotherapy agents on circulating leukocyte populations: Potential implications for the success of CAR-T cell therapies. *Cancers (Basel)* **13**, 2225 (2021).
83. M. Andreatta, S. J. Carmona, UCell: Robust and scalable single-cell gene signature scoring. *Comput. Struct. Biotechnol. J.* **19**, 3796–3798 (2021).
84. N. Borcherding, A. Vishwakarma, A. P. Voigt, A. Bellizzi, J. Kaplan, K. Nepple, A. K. Salem, R. W. Jenkins, Y. Zakharia, W. Zhang, Mapping the immune environment in clear cell renal carcinoma by single-cell genomics. *Commun. Biol.* **4**, 122 (2021).
85. A. M. Newman, C. L. Liu, M. R. Green, A. J. Gentles, W. Feng, Y. Xu, C. D. Hoang, M. Diehn, A. A. Alizadeh, Robust enumeration of cell subsets from tissue expression profiles. *Nat. Methods* **12**, 453–457 (2015).

86. Y. Zhu, B. L. Knolhoff, M. A. Meyer, T. M. Nywening, B. L. West, J. Luo, A. Wang-Gillam, S. P. Goedegebuure, D. C. Linehan, D. G. DeNardo, CSF1/CSF1R blockade reprograms tumor-infiltrating macrophages and improves response to T-cell checkpoint immunotherapy in pancreatic cancer models. *Cancer Res.* **74**, 5057–5069 (2014).

Acknowledgments
Funding: D.G.D. and study costs were supported by the National Cancer Institute R01CA273190, R01CA177670, R01CA203890, and P30CA09184215 and the Barnes-Jewish/Christian Cancer Frontier Fund. The project described was supported by T32HL007088 (to B.H.H.), T32 EB021955 (to L.-I.K.), and F31 DK122633 (to J.I.B.) from National Institutes of Health and award number K12 CA167540. **Author contributions:** B.H.H. and D.G.D. conceptualized the study. B.H.H., J.M.B., N.B., N.L.K., J.I.B., and G.D.H. developed the methodology. B.H.H., J.M.B., N.B., N.L.K., F.A., J.I.B., B.L.K., G.D.H., L.-I.K., J.P., C.-Y.L., R.G., and D.G.D. performed or assisted in the performance of the investigation of the study. B.H.H., J.M.B., N.B., N.L.K., and F.A. developed the visualization for the study. R.G. and D.G.D. supervised the study. B.H.H., J.M.B., N.L.K., R.G., and D.G.D. were responsible for writing the original draft and the revised final draft of the study. **Competing interests:** D.G.D. serves on the scientific advisory boards for OncoResponse, Adheare, and 149Bio. He also receives research support from BMS, Pfizer, and Verastem, all of which are unrelated to the current project. N.B. is a consultant for Santa Ana Bio Inc. and Omniscope Inc. All other authors declare that they have no competing interests. **Data and materials availability:** All data associated with this study are in the paper or the Supplementary Materials. scRNA-seq data are available via GEO accession number GSE227534.

Submitted 15 March 2023
Accepted 17 May 2023
Published 7 June 2023
10.1126/scitranslmed.adh8005